

MODELING AND MEASURING THE CHARACTERISTICS OF AN INDUCTIVELY  
COUPLED PLASMA ANTENNA FOR A MICRO-PROPULSION SYSTEM

by

Sonya Mary Christensen

A thesis

submitted in partial fulfillment

of the requirements for the degree of

Master of Science in Electrical Engineering

Boise State University

May 2012

© 2012

Sonya Mary Christensen

**ALL RIGHTS RESERVED**

BOISE STATE UNIVERSITY GRADUATE COLLEGE

**DEFENSE COMMITTEE AND FINAL READING APPROVALS**

of the thesis submitted by

Sonya Mary Christensen

Thesis Title: Modeling and Measuring the Characteristics of an Inductively Coupled Plasma Antenna for a Micro-Propulsion System

Date of Final Oral Examination: 14 March 2012

The following individuals read and discussed the thesis submitted by student Sonya Mary Christensen, and they evaluated her presentation and response to questions during the final oral examination. They found that the student passed the final oral examination.

Jim Browning, Ph.D. Chair, Supervisory Committee

Donald Plumlee, Ph.D. Member, Supervisory Committee

Wan Kuang, Ph.D. Member, Supervisory Committee

The final reading approval of the thesis was granted by Jim Browning, Ph.D., Chair of the Supervisory Committee. The thesis was approved for the Graduate College by John R. Pelton, Ph.D., Dean of the Graduate College.

## ACKNOWLEDGEMENTS

This work has been supported in part by NASA Grant #NNX09AV04A and Idaho Space Grant Consortium Grant #NNX10AM75H.

I would like to thank the following members of the EPROP Research team:

Dr. Don Plumlee and Dr. Jim Browning, who have guided this thesis.

Dr. Inanc Senocak, Dr. Sin Ming Loo, and Dr. Amy Moll, who all have provided resources and assistance to this thesis.

Carl Lee, who established the electrical system for operating the thruster. He collected much of the early plasma start data. He also wrote most of the LabView virtual instruments used in this thesis research.

Derek Reis, Jack Woldtvedt, Matt McCrink, Mallory Yates, Jesse Taff, Kelci Parrish, and Logan Knowles, who all worked in creating the physical devices to be tested, and in developing the mechanical systems for thruster operation and testing.

Peter Bumbarger, who assisted in the generation of the MATLAB simulation code, and collected the plasma start data after Carl Lee left the project.

It has taken a lot of effort from a lot of individuals for me to be able to complete this work. I would like to thank my advisor Dr. Jim Browning, for his patient guidance

from my sophomore year at Boise State University through the completion of my thesis. I would like to thank Donna Welch for reviewing my thesis. I would also like to thank Peter Bumbarger, Marcus Pearlman, and Jodi Chilson for their input as well.

I would like to thank Jayme Christensen, for being a source of encouragement and help when I need it. I would also like to thank the rest of my friends and family, for supporting me, offering advice, and giving me their unconditional love.

I would like to acknowledge Boise State University, which provided me with the tools I needed to pursue my education. I am amazed at the amount of knowledge I have accrued during my time here. The electrical engineering department has some very talented professors who clearly want to see students succeed, and care about the quality of graduates from their university.

I would like to acknowledge NASA, for providing assistance and encouragement to me and many other students like me.

I would like to acknowledge Micron, for intentionally fostering engineering excellence in Boise State's engineering program and the greater Boise area.

I would like to thank DuPont, for their work towards making their products affordable and accessible to Boise State University.

Finally, and most importantly, I would like to thank God for blessing me with so many opportunities and creating such an intricate and fascinating universe to explore.

## AUTOBIOGRAPHICAL SKETCH OF AUTHOR

Sonya Christensen graduated from Mountain View High School in Boise, Idaho. During high school she developed an interest in engineering, and participated in NASA's FIRST Robotics program with Mountain View's team.

At Boise State she became a student member of IEEE, and joined both Tau Beta Pi and Eta Kappa Nu. She was the Vice President of Boise State's chapter of Eta Kappa Nu her senior year. At the beginning of her sophomore year she became an undergraduate research assistant for Dr. Browning. In Dr. Browning's lab she worked on developing and fabricating a slow wave circuit for a Crossed-Field Amplifier. She also fabricated an energy analyzer to characterize the electrons going into the device.

During her sophomore year she was accepted as a NASA MUST scholar, and spent the following summer working at the Jet Propulsion Laboratory with the Deep Space Network. This experience fueled her interest in electromagnetics. After returning to Boise, she continued to work in Dr. Browning's Crossed-Field Amplifier group through her senior year, when she decided to pursue her Master's degree. Given her interest in electromagnetics and her background with NASA, this research project was a natural fit for her. She has greatly enjoyed working on this project and with the EPROP team at Boise State.

## ABSTRACT

An ion thruster for satellites on the order of 10-50 kg in mass is currently under development. The thruster uses an Inductively Coupled Plasma (ICP) generated by a flat spiral antenna fabricated using the Low Temperature Co-Fired Ceramic (LTCC) materials system. The antenna operating frequency range (600 MHz to 1 GHz) in LTCC ( $\epsilon_r=7.8$ ) results in a wavelength on the same order of magnitude as the total length of conductor in the antenna. This condition provides some interesting antenna electric and magnetic field characteristics. The antenna has been modeled using COMSOL Multiphysics® Simulation Software. By changing the geometry of the antenna in the model, the antenna design has been analyzed and improved. Two new antenna designs have been fabricated. The simulation results are compared to measurements of the antenna radio frequency (RF) electric field pattern. The simulation shows good agreement with the measurements.



## TABLE OF CONTENTS

ACKNOWLEDGEMENTS .....	iv
AUTOBIOGRAPHICAL SKETCH OF AUTHOR .....	vii
ABSTRACT.....	viii
LIST OF FIGURES .....	xii
LIST OF TABLES .....	xv
LIST OF ABBREVIATIONS.....	xvi
CHAPTER 1: INTRODUCTION .....	1
1.1    Research Description .....	1
1.1.3    Thesis Overview.....	2
CHAPTER 2: BACKGROUND .....	3
2.1    Propulsion .....	3
2.2    Electric Propulsion.....	4
2.2.1    Plasma Generation.....	7
2.3    General Thruster Design.....	10
2.3.1    Low Temperature Co-Fired Ceramic .....	12
2.4    Modeling.....	13
CHAPTER 3: SIMULATION .....	15
3.1    Antenna Model Geometry.....	15
3.1.1    COMSOL RF Coil Modeling.....	16

3.1.2	Simple Antenna Field Calculation .....	20
CHAPTER 4:	EXPERIMENTAL SETUP .....	23
4.1	ICP Source Setup .....	23
4.2	Fabrication Processes .....	24
4.3	Antenna RF Electric Field Measurement.....	26
4.4	Plasma Start Power Measurement .....	30
CHAPTER 5:	RESULTS, COMPARISON AND ANALYSIS .....	32
5.1	Simple Antenna Field Calculation .....	34
5.2	COMSOL Simulation .....	37
5.1.1	Model Verification .....	37
5.1.2	Design Parameter Analysis .....	38
5.1.3	New Antenna Designs.....	42
5.1.4	Analyzing Behavior of Low-Frequency Peak.....	54
5.1.4	Simulation Performance Comparison of Antennas $\alpha$ , $\beta$ , and $\gamma$ .....	56
CHAPTER 6:	CONCLUSIONS AND FUTURE WORK.....	58
6.1	Conclusions.....	58
6.2	Future Work .....	59
APPENDIX A.....		64
EPROP Research Group .....		64
APPENDIX B .....		65
COMSOL RF Simulation Model Development .....		65
APPENDIX C .....		73
SolidWorks Antenna Model Development.....		73

APPENDIX D.....	75
MATLAB Code .....	75

## LIST OF FIGURES

Figure 1. Diagram of Generic Ion thruster.....	6
Figure 2. Cross-section of the SolidWorks depiction of the entire thruster assembly.....	11
Figure 3. 3D solid model of antenna coil as seen in SolidWorks. ....	16
Figure 4. Mesh quality histogram as seen in the COMSOL user interface. ....	18
Figure 5. Effects of high quality mesh (top left) versus low quality mesh (top right), including high quality mesh histogram (bottom left) and low quality mesh histogram (bottom right) showing the quality of mesh vs. number of elements. ....	18
Figure 6. Spatially averaged electric field magnitude in the $E_x$ , $E_y$ , and $E_z$ directions, and total spatially averaged electric field intensity ( $E_{norm}$ ) [V/m] plotted vs. frequency.....	19
Figure 7. (a) [on left] Depiction of 5 phase-shifted loop antennas (b) [on right] Example of radiation pattern plot results from MATLAB simulation of circular loop antennas. Antennas are located at 0 on the y-axis, with the center of each loop at 0 on the x-axis.....	22
Figure 8. (a) [on left] Photograph of equipment used in the electrical setup for running the ion thruster (b) [on right] Block diagram of the electrical setup used to run the ion thruster. ....	24
Figure 9. Top view of ICP antenna fabricated on LTCC; with silver paste spiral conductor visible through the thin layer of LTCC; and SMA connector. ....	25
Figure 10. Magnified cross-section image of the ICP antenna on the LTCC substrate showing the silver paste trace under a thin layer of LTCC [22]......	26
Figure 11. Photograph of the Electric Field Measurement setup, showing the spectrum analyzer and XY stage. ....	27
Figure 12. Photograph of antenna mounted to the Teflon block on the XY stage, showing the RF connection and the dipole antenna probe centered above the antenna, perpendicular to the antenna surface. ....	28

Figure 13. Repeatability analysis of XY stage measurements. Top: electric field measurement of an antenna, Middle: repeated electric field measurement of an antenna, Bottom: the difference between the two measurements. Left: false color plots showing each data point taken, Right: histograms of the data. ....	29
Figure 14. Photograph of an ICP discharge showing LTCC antenna structure on a Teflon stand with gas inlet connection. ....	30
Figure 15. Inverted, normalized plasma start power at 500 mTorr and normalized, spatially averaged, measured, antenna electric field for antenna $\alpha$ . ....	34
Figure 16. Field radiation pattern result of the phase-shifted loop approximation of the spiral antenna. ....	36
Figure 17. Measured and simulated electric field intensity ratios for antenna $\alpha$ , normalized to the 923 MHz case. ....	38
Figure 18. Simulated electric field intensity for antenna in LTCC ( $\epsilon_r=7.8$ ) and in air ( $\epsilon_r=1$ ). ....	39
Figure 19. Simulated average electric field intensity vs. frequency for antenna $\alpha$ design and for a deeper electrical via. ....	41
Figure 20. Simulated average electric field intensity vs. frequency for antenna $\alpha$ , and for a wider conductor trace. ....	41
Figure 21. Simulated average electric field intensity vs. frequency for 5, 7, 9, and 11 turn antennas, all with an outer diameter of approximately 15mm. ....	43
Figure 22. Measured and simulated electric field intensity ratios for antenna $\gamma$ , measured data is normalized to the 727 MHz case, simulated data is normalized to the 730 MHz case. ....	45
Figure 23. Measured and simulated electric field intensity ratios for antenna $\beta$ , measured data is normalized to the 805 MHz case, simulated data is normalized to the 500 MHz case. ....	45
Figure 24. Contours of experimentally measured electric field intensity for antenna $\alpha$ , normalized to the 923 MHz case. ....	48
Figure 25. Contours of simulated electric field intensity for antenna $\alpha$ , normalized to the 923 MHz case. ....	49
Figure 26. Contours of experimentally measured electric field intensity for antenna $\beta$ , normalized to the 757 MHz case. ....	50

Figure 27. Contours of the simulated electric field intensity for antenna $\beta$ , normalized to the 757 MHz case.....	51
Figure 28. Contours of experimentally measured electric field intensity for antenna $\gamma$ , normalized to the 727 MHz case. ....	52
Figure 29. Contours of simulated electric field intensity for antenna $\gamma$ , normalized to the 730 MHz case. ....	53
Figure 30. Comparison of simulated average electric field intensities for antennas $\beta$ , $\delta$ , $\epsilon$ , and $\eta$ , not normalized.....	55
Figure 31. Comparison of simulated average electric field intensities for antennas $\alpha$ , $\beta$ , and $\gamma$ , normalized to antenna $\alpha$ 923 MHz case. ....	57
Figure A.1. EPROP Research Group. From left to right: Logan Knowles, Sonya Christensen (the author), Don Plumlee, Jim Browning, Matt McCrink, Sin Ming Loo, Carl Lee, Jack Woldtvedt, Inanc Senocak. The vacuum chamber is in between Drs. Plumlee and Browning. Not pictured: Mallory Yates, Peter Bumbarger, Jesse Taff, Derek Reis, Kelci Parrish, Dr. Amy Moll.....	64
Figure B1. Basic RF coil model.....	66
Figure B2. Example of right-clicking while hovering over “Geometry” to show the import option.....	67
Figure B3. Creating the rectangle to be used as the lumped port .....	68
Figure B4. LTCC domain Wave Equation settings .....	69
Figure B5. Lumped Port settings .....	70
Figure B6. Mesh details for antenna $\beta$ .....	71
Figure B7. Viewing and exporting results .....	72
Figure C1. SolidWorks antenna development .....	73

## LIST OF TABLES

Table 1: List of antennas analyzed for lower-frequency peak .....	55
Table C1: List of antennas simulated and fabricated .....	73

## LIST OF ABBREVIATIONS

RF	Radio Frequency
ICP	Inductively Coupled Plasma
LTCC	Low Temperature Co-Fired Ceramic
PML	Perfectly Matched Layer
XY stage	X-axis and Y-axis movement stage
Peak frequency	frequency corresponding to largest average electric field
EPROP	Electric Propulsion Group at Boise State



## CHAPTER 1: INTRODUCTION

### 1.1 Research Description

An antenna was fabricated using DuPont 951 Green Tape Low Temperature Co-Fired Ceramic (LTCC) [1] to be used as an Inductively Coupled Plasma (ICP) source [2]. LTCC is a novel dielectric material with good thermal and electrical characteristics [1]. The wavelength of the spiral antenna is on the same order of magnitude as the total length of conductor in the antenna. This condition provides some interesting electric and magnetic field characteristics. To improve the design, the antenna was simulated in COMSOL Multiphysics® Simulation Software. The model was verified experimentally.

The antenna is intended to be used in an ion thruster for satellites 10 kg-50 kg in mass. Ion thrusters use ions accelerated by electric fields to generate thrust. Because small satellites carry a limited amount of propellant, a high fraction of ionization (90%-100% of propellant particles) at a reasonably low power and low ambient pressure is desirable. The flat spiral antenna design must provide high fields at the operating frequency in order to obtain a high fraction of ionization. Various geometries have been simulated to determine the effects of varying antenna characteristics such as the conductor trace width, conductor trace thickness, pitch, and the number of turns. This thesis provides a design and analysis of the antenna through simulation and comparison to experiments.

### 1.1.3 Thesis Overview

The objective of this thesis is to model and design the antenna for an ion propulsion device. The purpose of modeling the antenna is to provide an improved design and provide some explanations for the experimental results obtained.

Chapter 2 provides the background of electric propulsion, discusses different types of electric propulsion systems, and presents reasons for the thruster design choice. Chapter 3 describes the simulation software and approach for determining the antenna fields, plasma generation, and thruster body. Chapter 4 describes the experimental approach, including antenna field measurements, and plasma data. Chapter 5 provides a detailed description of the results and a comparison of the techniques in the previous two chapters. Chapter 6 provides a summary of the work done and recommendations for future work.

## CHAPTER 2: BACKGROUND

### 2.1 Propulsion

There are two primary categories for spacecraft propulsion: Chemical Propulsion and Electric Propulsion. Chemical propulsion devices generate thrust by ejecting a propellant mass at high velocity from a nozzle. The energy in the flow is obtained through a chemical reaction in the propellant. Types of chemical propulsion devices include Biopropellant Thrusters, Monopropellant Thrusters, Cold Gas Thrusters, Tripropellant/Warm Gas Thrusters, Solid Rocket Motors, and Hybrid Rocket Motors [3]. Electric propulsion devices generate thrust by extracting the propellant mass at high velocities through the use of electric fields. Types of electric propulsion devices include Ion Engines, Hall Thrusters, Field Emission Electric Propulsion (FEEP), Colloid Thrusters, Pulsed Plasma Thrusters, Resistojets, Arcjets, and Magnetoplasmadynamic Thrusters [3, 4]. Thrusters are often compared using two basic parameters: thrust and specific impulse.

Thrust is a force and is defined by the following equation (Eq. 1).

$$T = \dot{m}v \quad (\text{Eq. 1})$$

where:  $T$  = generated thrust [N]

$\dot{m}$  = mass flow rate of propellant leaving thruster [kg/s]

$v$  = velocity of exiting mass [m/s]

Specific impulse is a measurement of the efficiency of a thruster and is defined by the following equation (Eq. 2).

$$I_{sp} = \frac{T}{\dot{m}g_0} \quad (\text{Eq. 2})$$

where:  $I_{sp}$  = specific impulse [s]

$T$  = thrust [N]

$\dot{m}$  = propellant mass flow rate [kg/s]

$g_0$  = acceleration of earth gravity [ $\text{m/s}^2$ ]

Because of the nature of the two propulsion types, electric propulsion tends to have much greater specific impulses than chemical propulsion due to higher velocity. Most chemical propulsion devices have a specific impulse less than 300 s; whereas Ion Engine designs have specific impulses near or above 2000 s [3]. The efficient use of propellant is critical to thrusters for small satellites. Because of these reasons, electric propulsion is generally better suited to in-space applications than chemical propulsion, despite having lower mass flow rates and, thus, lower thrust. To maximize the use of the propellant in electric propulsion, high fractions of ionization of the neutral gas and high ionization rates are required to ensure that few unionized molecules escape the thruster.

## 2.2 Electric Propulsion

Within electric propulsion there are many devices, each with its own benefits and drawbacks. Ion Engines and Hall Thrusters are two types of electric propulsion that have been used for space applications, and the operational concepts are useful for

understanding the physics behind the design chosen for this thesis research. The propulsion device for this thesis is of an Ion Engine type (also called an Ion Thruster).

### Ion Engine

Ion Engines consist of four fundamental components: a discharge cathode, a discharge chamber, ion optics, and a neutralizer cathode, as shown in Figure 1. Magnets may also be added to improve the thruster performance. The propellant is ionized in the discharge chamber by electrons from the discharge cathode. Then, the ions are accelerated out of the device by the ion optics to provide thrust. The ion optics consist of two or three electrostatic grids that extract and accelerate the ions: a screen grid and one or two accelerator grids. To prevent a charge differential between the spacecraft and the extracted ions, the ions are neutralized with electrons after they exit the discharge chamber. Neutralizers are electron sources external to the discharger chamber. One such electron source is a hollow cathode electron source. A hollow cathode electron source can generate electrons by thermionic emission in which a cathode is heated to a temperature where electrons will be emitted as described by Eq. 3 [5, 6]. A hollow cathode can also be used as a discharge cathode for a DC glow discharge, as is described in Section 2.2.1. The current density from a thermionic cathode is given by:

$$J = A_0 T^2 e^{-\frac{\phi_m}{kT}} \quad (\text{Eq. 3})$$

where:  $J$  = current density [A/cm<sup>2</sup>]

$A_0$  = thermionic emission constant = 120 A/cm<sup>2</sup>/K<sup>2</sup>

$\phi_m$  = metal work function [eV]

$T$  = absolute temperature [K]

$k$  = Boltzmann's constant =  $1.38 \times 10^{-23}$  [J/K]

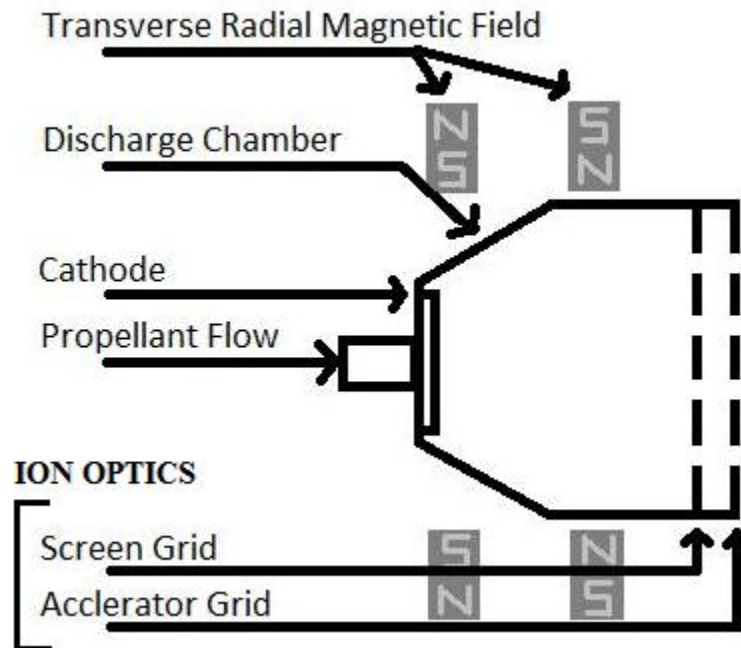


**Figure 1. Diagram of Generic Ion thruster**

In 1998, NASA launched the Deep Space 1 spacecraft. The NASA Solar Electric Propulsion Technology Application Readiness (NSTAR) program was responsible for the development of an ion thruster for this mission: the first to rely on solar electric propulsion as the primary propulsion system [7]. The flight thruster was 30 cm in diameter and used xenon gas as propellant. The xenon ions are accelerated by the ion optics, which consists of a screen grid that is set to the discharge chamber common voltage, and an accelerator grid set to a voltage between -150 V and -250 V. From the neutralizer electric potential, the discharge chamber can be biased up to 1100 V, which

accelerates the positive ions out of the chamber. This thruster design is capable of providing thrust in the range of 20-92 mN with a specific impulse of 1950-3100 s [8].

### Hall Thruster

Hall thrusters consist of three main components: a discharge chamber, a cathode, and a magnet system. The discharge chamber is a ring-shaped structure, and the cathode is located just outside of the exit. Electrons from the cathode are accelerated into the discharge chamber by an electric field generated from an anode plate on the opposite side of the exit. The electrons spin around the ring due to the magnetic field and ionize the propellant. The resulting azimuthal current is called the Hall current [4]. The ions are accelerated out of the discharge chamber by an electric field generated by the same anode and are neutralized by a portion of the electrons from the cathode as it exits the thruster [4].

The European Space Agency launched SMART-1 on September 27, 2003 [9]. The spacecraft used a PPS® 1350-G Hall effect plasma thruster. This device was developed by Snecma and is largely based on the Russian SPT-100 technology [10]. This thruster was also powered with solar energy and used xenon as a propellant. The SMART-1 measured thrust was around 50 mN, and the specific impulse was around 1600 s [9].

#### 2.2.1 Plasma Generation

In order to provide thrust, all electric propulsion devices need a source of charged particles. For ion and Hall thrusters, plasmas provide these particles. There are a few

main types of plasma discharges: Wave Heated Discharges, Direct Current (DC) Discharges, Capacitive Discharges, and Inductive Discharges [6].

In Wave Heated plasmas, radio or microwave frequency radiation is injected into the thruster chamber to ionize the neutral gas and sustain the plasma discharge. Some stray electrons already in the chamber are excited by the radiated waves and are accelerated by the wave electric field. If the pressure, frequency, and microwave power are felicitous, the electrons will undergo electron-impact ionization (an ionizing collision in which an atom is separated into an ion and an electron). For a plasma to be sustainable, the rate of ionizing collisions must balance out loss rates from other collisions (such as with the chamber/thruster wall). During plasma initiation, the fraction of ionization is low, which causes more non-ionizing collisions to occur. Because of this higher loss rate, a higher microwave power is required to initiate plasma.

A basic DC Glow Discharge is generated using an anode and cathode with neutral gas placed between the two. The anode and cathode create an electric field that accelerates stray electrons in the neutral gas. If the gas density and the electric field are appropriate, this acceleration of electrons in the gas results in ionizing collisions [6]. As more collisions take place, more electrons are available to undergo ionizing collisions. Eventually the density of charged particles in the plasma can shield particles from the electric field, but at either end of the plasma there is a region where the particles still see an electric field. This is called the sheath region of the plasma. In a DC discharge, the voltage drop near the cathode is higher than the voltage drop near the anode. In a discharge source such as the one used in the NSTAR Ion Engine, the electrons for the DC Discharge come from a hollow cathode discharge. This source of electrons reduces the



potential required for breakdown and initiation of the discharge by increasing the chance of ionizing collisions.

In Capacitive Discharges, an electrode is placed in a neutral gas. Instead of a high DC voltage bias, a time varying signal (RF wave, typically 13.56 MHz) is applied to the electrode relative to a designated ground potential [6]. The electric fields generated by the electrode create a sinusoidal current within the bulk of the plasma. At the plasma sheaths, this current is sustained primarily as a displacement current (current due to a time-varying electric field) rather than conductive [6]. Displacement current is caused by the time varying electric field as seen across the sheath and is described by Eq. 4.

$$I = \epsilon_0 A \frac{\delta E}{\delta t} \quad (\text{Eq. 4})$$

where:

$I$ = displacement current [A]

$E$ = electric field [V/m]

$A$  = surface area of electrode [m<sup>2</sup>]

$\epsilon_0$ = permittivity of free space [F/m]

$t$ = time [s]

An inductively coupled plasma (ICP) source uses a radio frequency signal (typically 13.56 MHz) applied to an antenna that is not exposed in the plasma chamber [6]. The RF fields that sustain the plasma are magnetic and come from the coils of the inductor. These time-varying magnetic fields induce an electric field. This type of plasma source can be modeled as a transformer; in fact it is sometimes referred to as a transformer-coupled plasma. Inductively coupled plasmas are known to generate high-

density ( $\sim 10^{12}$  particles/m<sup>3</sup>), low-pressure plasmas (<50 mTorr), and thus, are a good choice for an Ion Thruster [6]. Miniature ICP devices were demonstrated by Hopwood [2, 11-14] and detailed descriptions of the design, testing, and analysis of ICPs can be found in that work.

### 2.3 General Thruster Design

The goal of the EPROP team is to design and fabricate a thruster for small satellite propulsion. The thruster for this project is an Ion Engine design that uses an Inductively Coupled Plasma (ICP). An Ion Engine design is well-suited to this application because of the high specific impulse, the obtainable 200  $\mu$ N thrust for small satellites, and the suitability for the fabrication process [3]. Ion thrusters require an ion source. For a small thruster that requires a high-density plasma (for efficient use of propellant), an ICP is the best choice. ICP's were discussed in further detail in Section 2.2.1. The ICP is generated by a flat spiral antenna that is operated in the 500 MHz to 1 GHz range. This plasma generation is well-suited to small satellite application because ICP's are generally higher density than the other plasma discharge types, and LTCC can protect the antenna from erosion caused by the plasma bombardment.

The design for the thruster for this project is shown in Figure 2. The thruster body consists of an LTCC tube 2 cm in diameter and 1.5 cm tall [15]. Argon is the propellant and is provided to the thruster at a mass flow rate of 0-23 sccm from a gas inlet in the center of the antenna. The project uses an LTCC body for the thruster rather than a conductor (like NSTAR uses) because the ICP is generated by an RF antenna covered by a dielectric. In the NSTAR design the thruster body is biased to a high potential. In the LTCC thruster design the thruster wall is dielectric, so the thruster body cannot be biased

to generate an accelerating electric field. Instead, the antenna used to generate the ICP is set to ground. This approach is preferable, as biasing the antenna to a high negative voltage is not a practical design choice. Two grids are then placed on top of the thruster body: the grid closest to the antenna (screen grid) is biased at 1000 V, and the grid farthest from the antenna (acceleration grid) is biased at -200 V. The grids are the only exposed conductor, so the plasma will be biased up to that potential; in fact, the bulk plasma will be slightly above that potential because the negatively charged electrons leave the plasma more quickly than positively charged ions. The slight negative voltage on the acceleration grid helps to keep electrons from the neutralizer from moving into the thruster body.

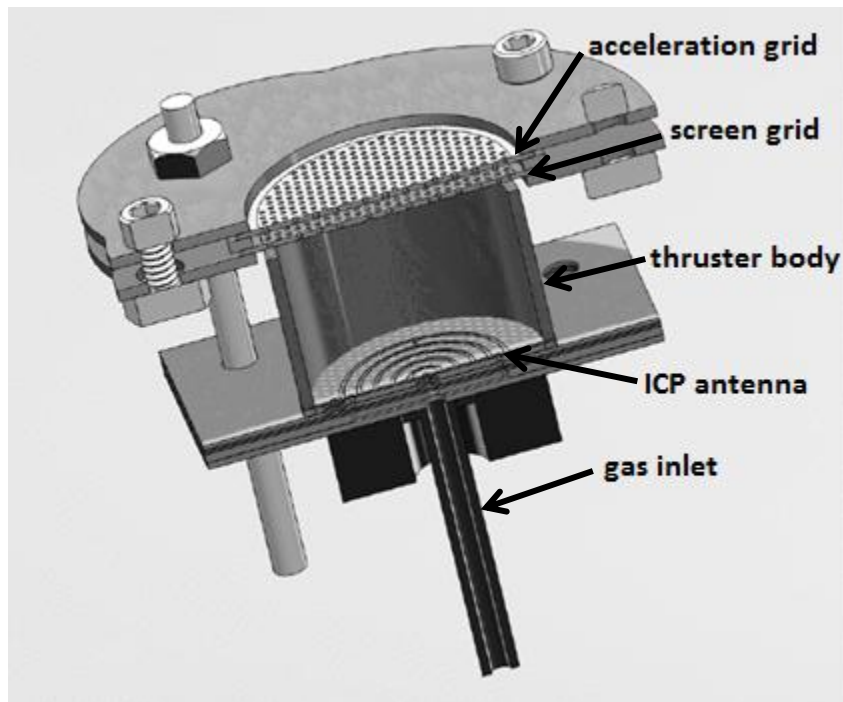


**Figure 2. Cross-section of the SolidWorks depiction of the entire thruster assembly.**

The antenna for the thruster is a flat spiral design embedded in the LTCC. The ability of this antenna to light a plasma had already been demonstrated by the EPROP team (Appendix A) prior to the start of the simulation work. In addition, this antenna was tested for its usefulness in assisting plasma ignition in a Pulsed Inductive Plasma Thruster design at Marshall Space Flight Center in November, 2011.

### 2.3.1 Low Temperature Co-Fired Ceramic

LTCC is a novel material that is manufactured at DuPont [1]. It is a good high frequency electrical material with a permittivity of 7.8 at 3 GHz. The unfired LTCC comes in sheets. The sheets are cut (typically with a laser) to the desired shapes and laminated together. At this point any desired machining can take place, and conductive materials can be applied to the LTCC tape surfaces. Conductive materials can either be screen printed onto the LTCC or deposited by using a direct write tool. If the structure consists of multiple pieces, these pieces must be assembled and laminated under pressure. For this device, all but the top layer of LTCC is assembled, and the device is pressed at 70° C and 1.37 MPa for 5 minutes. Next, the top layer of LTCC is added; then, the device is pressed again at 70° C and 19.2 MPa for 10 minutes. Then, the LTCC is fired in a furnace at a temperature of 350° C for binder burn out, and then at 850° C for liquid phase sintering [16]. The result is a blue ceramic piece that can contain various electrical components, such as the antenna for inductively coupled plasma generation. The fabrication process also allows for interlayer communication using electrical vias. LTCC is very versatile, resistant to plasma erosion, and thermally resistant; therefore, it is well-

suited to the thruster application [17]. A description of the specific fabrication process used for this project is given in Section 4.1.

## 2.4 Modeling

COMSOL Multiphysics® Simulation Software was used to analyze the antenna for this thesis [18]. COMSOL was initially released under the name FEMLAB because it uses the Finite Element Method (FEM) to solve partial differential equations. FEM is capable of analyzing the wave equation in both driven and undriven geometries. FEM works by taking the initial partial differential equations and changing them to a so-called “weak” form, which can be used to evaluate each of the elements separately [19].

For the antenna analysis, the RF Module was used; this module solves the wave equation as shown in Eq. 5. After the wave equation was solved in COMSOL, the electric field intensity was compared between antenna models. The highest electric field intensity above the antenna indicates the best performing model. For the purposes of this research, the wave equation solved by COMSOL is given by:

$$\nabla \times \mu_r^{-1}(\nabla \times \mathbf{E}) - k_0^2 \left( \epsilon_r - \frac{j\sigma}{\omega\epsilon_0} \right) \mathbf{E} = 0 \quad (\text{Eq. 5})$$

where:

$\mu_r$ = relative permeability of material

$\mathbf{E}$ = electric field [V/m]

$k_0$  = wavenumber [ $\text{m}^{-1}$ ]

$\epsilon_r$ = relative permittivity of the material

$\sigma$ = conductivity of material [S/m]

$\omega$  = angular frequency [rad/s]

$\epsilon_0$  = permittivity of free space [F/m]

$$j = \sqrt{-1}$$

## CHAPTER 3: SIMULATION

The goal of the simulation of the antenna was to design an antenna to generate the highest RF fields directly above the antenna by changing the antenna geometry and operating frequency. This high field in turn generates higher density plasma and provides lower plasma initiation powers. A lower plasma initiation power indicates a better performing thruster.

### 3.1 Antenna Model Geometry

When simulation work began, the primary goal was to model an antenna design that was already found to work experimentally. The design was for a five-turn, 0.9 mm pitch flat spiral antenna embedded 35  $\mu\text{m}$  deep in a 1.4 mm thick piece of LTCC; this antenna is called antenna  $\alpha$ . The antenna's input is from a side-mount SMA connector, so the traces that led to the antenna coil are placed accordingly. The conductor in the antenna was constructed as a 3D solid model in SolidWorks, as seen in Figure 3. Once verification of the model could be obtained, work to improve the antenna design based on modeling different parameters began.



**Figure 3. 3D solid model of antenna coil as seen in SolidWorks.**

### 3.1.1 COMSOL RF Coil Modeling

To begin the simulation process, the antenna  $\alpha$  coil design was drawn in SolidWorks and imported to COMSOL. This step was needed because originally COMSOL's CAD environment was unable to generate a flat spiral shape. In COMSOL, the antenna was embedded in a rectangle or cylinder the thickness of the LTCC. Then, a lumped port was added to excite the antenna. In COMSOL, a lumped port functions as a voltage supply, matched to a user-specified value. The value was set to 1 V and matched at 50  $\Omega$ . For the simulation, the entire assembly was embedded into a sphere of air with a Perfectly Matched Layer (PML) at the boundary. The Perfectly Matched Layer is a COMSOL modeling tool that mimics a boundary that is infinitely far away. The entire model, except for the coil surface, was left as air. The coil surface was given an impedance boundary condition that referenced a high conductivity material. To achieve the desired physics in the LTCC domain, a separate wave equation analysis was applied to that region, with  $\epsilon_r=7.8$  and a loss tangent  $\delta=0.006$ , which mimics the properties of LTCC. The model was then meshed with a free tetrahedral mesh over the entire



assembly except for the PML. In the PML, a swept mesh was used to ensure any possible reflections from the simulation boundary would be attenuated. Meshing the spiral antenna within the LTCC was not simple, as the very thin layer of LTCC above the antenna along with the relatively large overall geometry caused the number of elements to become much too large if the right constraints were not applied to the mesh. Details of the creation of the COMSOL model file and SolidWorks geometry file are shown in Appendices B and C, respectively.

The mesh was analyzed for quality in COMSOL. Quality is how well a particular mesh represents the geometry being modeled. A typical element quality distribution from COMSOL is shown in Figure 4. The x-axis is the quality of the element from 0 to 1. The y-axis shows the number of elements at each quality level. Low quality elements are assigned a value of 0, and high quality elements are assigned a value of 1. It can be seen that there are some low quality elements, which could affect the simulation results. A comparison was done to verify that these low quality elements did not in fact make the simulations invalid. Figure 5 has two simulations of one geometry: one with a low quality mesh and one with a high quality mesh. The fields in the low quality mesh can be seen to have some noise, but the overall field is the same as the high quality mesh version.

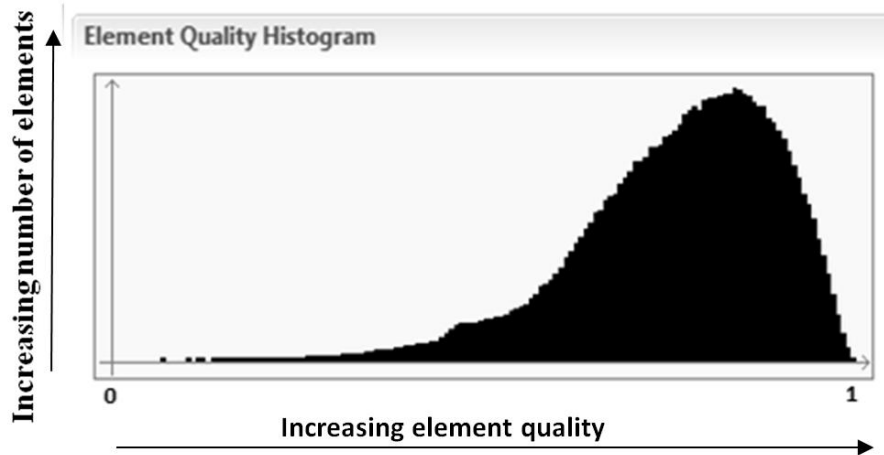


Figure 4. Mesh quality histogram as seen in the COMSOL user interface.

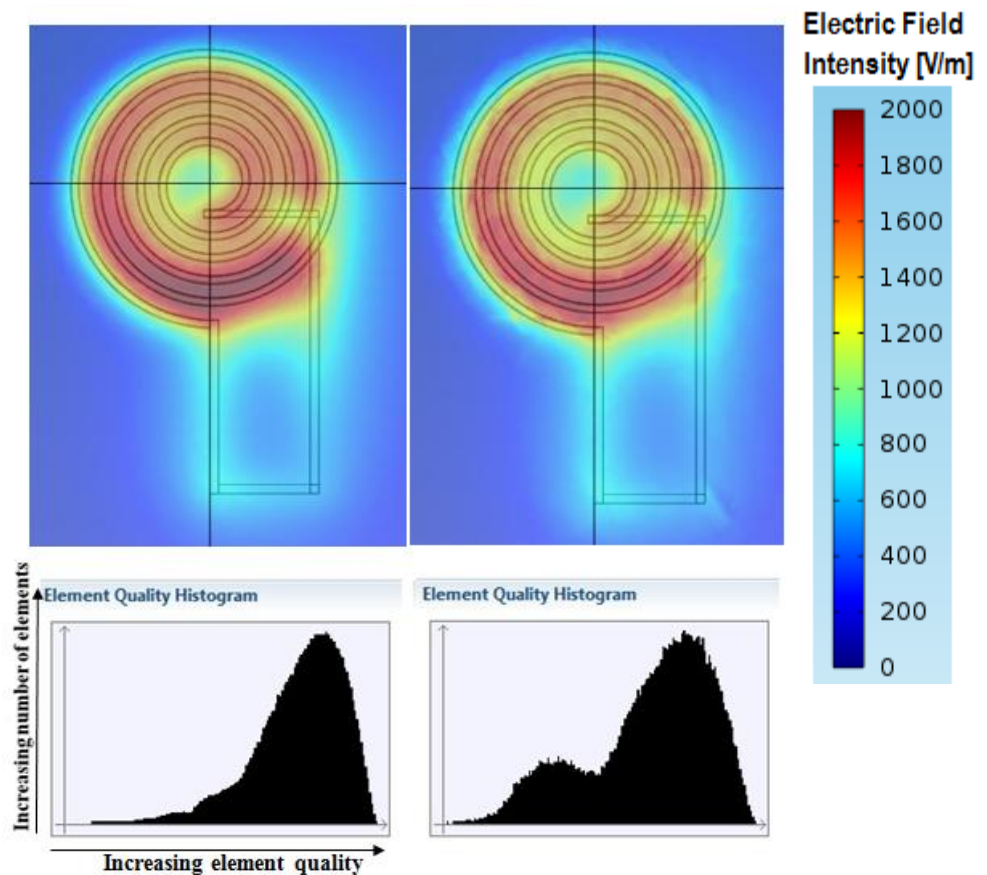
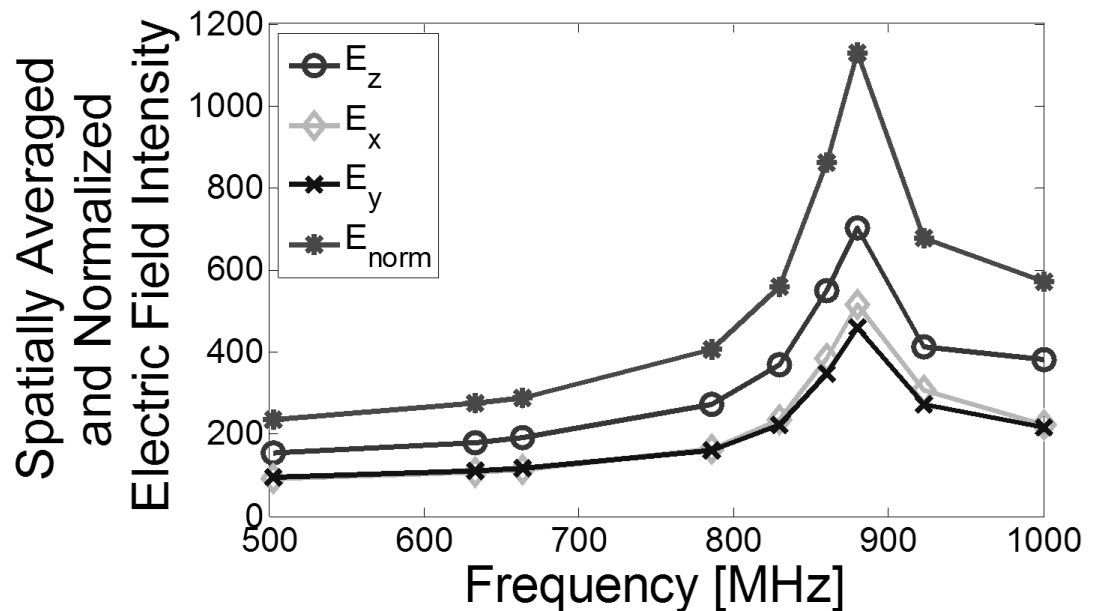


Figure 5. Effects of high quality mesh (top left) versus low quality mesh (top right), including high quality mesh histogram (bottom left) and low quality mesh histogram (bottom right) showing the quality of mesh vs. number of elements.

After model verification, several different antenna designs were generated in SolidWorks for comparison to the original design. The designs were then run in the same configuration as the original antenna in COMSOL. Data points for electric field intensity and magnetic field intensity at 1 mm above the surface of the LTCC were imported into MATLAB [20]. Once in MATLAB, the data points were averaged and the average fields were plotted vs. frequency, as is shown in Figure 6. The figure shows different spatial components of the RF electric field. To initially analyze the antenna's electric field characteristics, each field direction was analyzed. It was determined that the electric field perpendicular to the antenna surface ( $E_z$ ) was dominant, and that all directions show similar changes vs. frequency. For the remaining analysis of the antenna, the total spatially averaged electric field intensity ( $E_{norm}$ ) was used. The data is also shown as a plot of intensity vs. position above the antenna in Chapter 5.



**Figure 6. Spatially averaged electric field magnitude in the  $E_x$ ,  $E_y$ , and  $E_z$  directions, and total spatially averaged electric field intensity ( $E_{norm}$ ) [V/m] plotted vs. frequency.**

### 3.1.2 Simple Antenna Field Calculation

Using Eq. 6-9 from Antenna Theory Analysis and Design by Constantine A. Balanis [21], a simplified near-field radiation plot of the fields vs. frequency for each design could be generated using MATLAB. This calculation was performed in order to provide some understanding of the behavior of the antenna when it operates with a wavelength comparable to the total conductor length. The antenna near-field equations for a circular loop antenna are given by:

$$H_r = \frac{a^2 I_0 e^{-jkr}}{2r^3} \cos \theta \quad (\text{Eq. 6})$$

$$H_\theta = \frac{a^2 I_0 e^{-jkr}}{4r^3} \sin \theta \quad (\text{Eq. 7})$$

$$E_\phi = -j \frac{a^2 I_0 e^{-jkr}}{4r^2} \sin \theta \quad (\text{Eq. 8})$$

$$H_\phi = E_r = E_\theta = 0 \quad (\text{Eq. 9})$$

where:

$E$  = electric field [V/m]

$H$  = magnetic field [A/m]

$k$  = wavenumber [ $\text{m}^{-1}$ ]

$I_0$  = magnitude of current in loop [A]

$a$  = radius of loop [m]

$j = \sqrt{-1}$

$r, \theta, \phi$  = spherical coordinates [m, rad (inclination), rad (azimuth)]

To apply the above equations to the antenna, it was assumed the antenna consisted of phase shifted loops of evenly increasing radii, and the fields were summed to create a total field. This approach is shown in Figure 7(a). The signal was considered to be applied to the outermost loop first, with no phase shift. The second loop from the outside was considered to receive the signal second, so a phase shift that corresponded to the applied wavelength divided by the diameter of the outermost loop was used. The third loop from the outside received a phase shift that corresponded to the applied wavelength divided by the summed diameters of the first and second loops. This process continued for every loop in the antenna. The total fields were then summed, and the results are plotted on a radiation plot as are shown in Figure 7(b). The equations were manipulated to include the phase shift, so that the ratio of the loop radii to the wavelength of the applied signal was the relevant characteristic, and so that MATLAB properly computed the exponential powers. Complete results from the cases modeled are in Chapter 5, and the code used to run the model is in Appendix D.

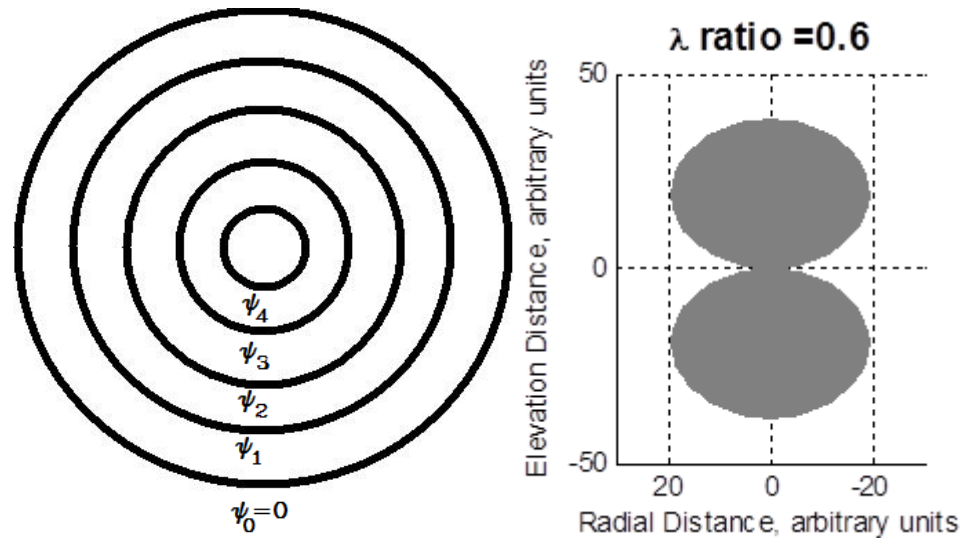


**Figure 7. (a) [on left] Depiction of 5 phase-shifted loop antennas (b) [on right] Example of radiation pattern plot results from MATLAB simulation of circular loop antennas. Antennas are located at 0 on the y-axis, with the center of each loop at 0 on the x-axis.**

## CHAPTER 4: EXPERIMENTAL SETUP

The purpose of experimental analysis of the antenna is to demonstrate the functionality of the device and to provide validation for the simulated analysis. The plasma start data demonstrates the functionality, and the electric field measurement provides the validation of the simulation results. Both experiments use much of the same equipment, as is described in Sections 4.1 through 4.4.

### 4.1 ICP Source Setup

The ICP source experiments were conducted in a 75 cm long by 58 cm diameter vacuum chamber that was repurposed from a semiconductor processing sputtering device. To conduct the experiment, a thruster mounting block fabricated from Teflon is placed in the chamber, upon which the antenna is attached. The RF power is routed to the antenna through a connection on the vacuum chamber. The power is supplied by an Empower RF Systems 2021-BBS2E4AHM 20-1000 MHz, 50 W high power RF Amplifier. To initiate plasma, an RF coupler and isolator are placed in line to measure the forward and reflected power and to prevent the reflected power from damaging the RF amplifier. To test the antenna, it must first be matched to the RF source. This matching is performed with a matching network that consists of 4 variable (0.6-4.5 pF) capacitors. Three of the capacitors are connected in parallel and one is connected in series. Using a Hewlett-Packard 8712C 300 kHz-1300 MHz RF Network Analyzer, the matching network is tuned to a characteristic impedance of 50  $\Omega$ . A full block diagram

of the electrical experimental setup is shown in Figure 8 (b), and a photograph of the equipment is shown in Figure 8 (a). The plasma measurements were performed by the EPROP Group.

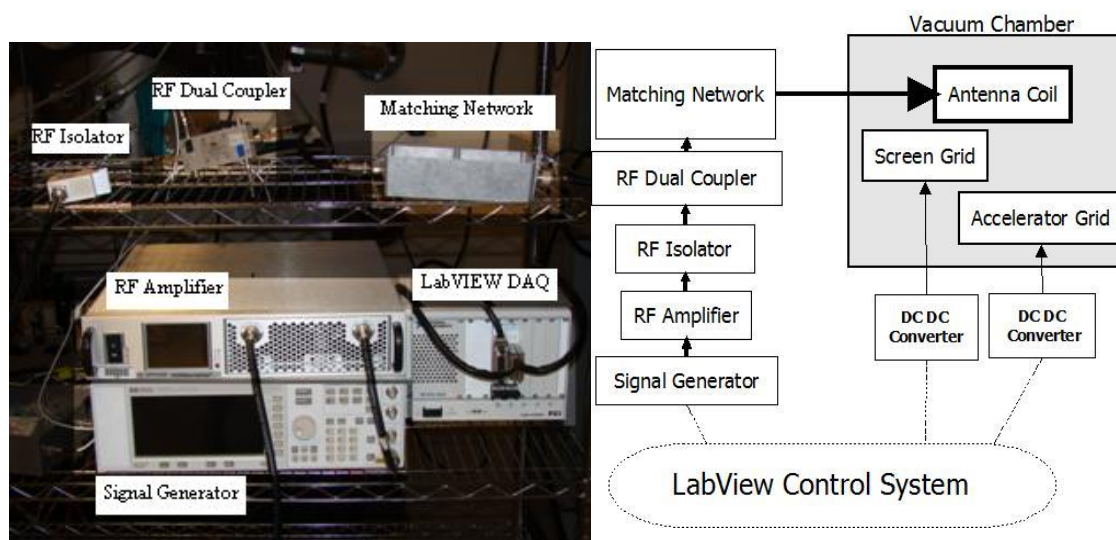


**Figure 8. (a) [on left] Photograph of equipment used in the electrical setup for running the ion thruster (b) [on right] Block diagram of the electrical setup used to run the ion thruster.**

## 4.2 Fabrication Processes

The antennas were fabricated in LTCC by the EPROP Group. The LTCC comes in sheets from DuPont. For the 1.2 mm thick LTCC piece, the LTCC is cut into six pieces from DuPont's 951PX LTCC, each with the same mounting holes, gas inlet, and electrical via holes. The pieces are stacked and laminated. In the lamination process the LTCC piece is pressed at 1.37 MPa and 70° C for 5 to 10 minutes. Next, the conductor for the antenna is applied with an nScript 150-3Dn-HP micro-dispensing pump using DuPont's 6145 Silver Conductive paste, and a final sheet of DuPont's 951P2 LTCC (50.8  $\mu\text{m}$  thick pre-firing) is placed on top of the conductor. The entire assembly is fired in a Lindberg/Blue M BF51828C-1 Box Furnace according to the profile provided by



DuPont, which includes heating the piece to 350° C so that the organic binder may be burned out, then heating the piece up to 850° C to lock the alumina in the glass matrix. Then, the furnace is allowed to slowly cool. Finally, an SMA connector is attached on the edge of the LTCC using a silver epoxy [16]. An example of a fabricated antenna is shown in Figure 9, and a cross-section of the coil showing a single conductor trace is shown in Figure 10. The fabricated antenna is 5 turns with a 0.9 mm pitch from a 2.5 mm starting diameter. The conductor that makes up the coil is flattened during fabrication, which results in a maximum trace width of 0.36 mm and a maximum thickness of 0.06 mm. The thin LTCC over the antenna both increases the effective permittivity on applied signals and protects the antenna from plasma bombardment. For all data shown in this thesis, the antenna is assumed to be oriented as shown in Figure 9 with the SMA connector at the bottom of the page.

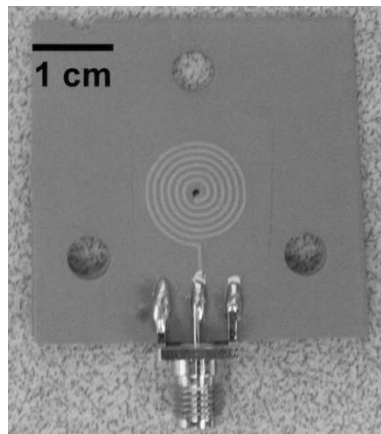


**Figure 9. Top view of ICP antenna fabricated on LTCC; with silver paste spiral conductor visible through the thin layer of LTCC; and SMA connector.**

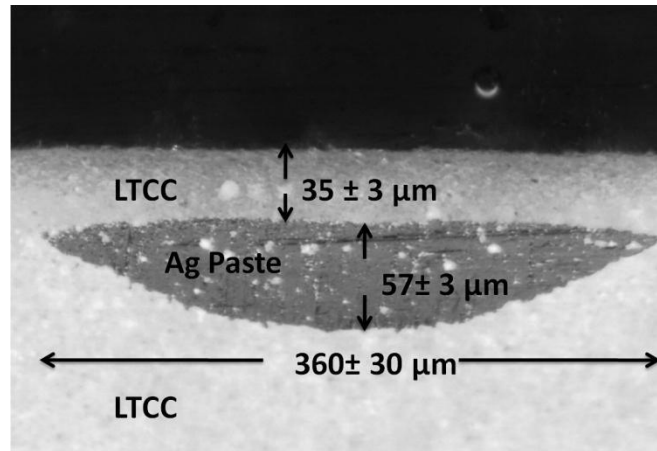


**Figure 10. Magnified cross-section image of the ICP antenna on the LTCC substrate showing the silver paste trace under a thin layer of LTCC [22].**

### 4.3 Antenna RF Electric Field Measurement

In order to measure the RF electric field, the antenna is placed on a stage outside of the chamber with two servos that move the stage in the x and y directions. A coaxial cable connects the source to the matching network and the matching network to the antenna. A Hewlett-Packard E4411B 9 kHz-1.5 GHz ESA-L Series Spectrum Analyzer sits next to the stage and is connected to a coaxial cable set up as a receiving dipole antenna that is placed 1 mm above the ICP antenna, as is shown in Figure 11. Using a LABVIEW virtual interface, the receiving antenna is positioned directly above the center of the ICP antenna as a reference point, as shown in Figure 12. Then, a 20 dBm RF signal is sent to the ICP antenna. The test is set to cover a square area over the antenna with a user-determined resolution. For the 15 mm diameter antennas, this area was determined to be  $19.05 \times 19.05$  mm with a resolution of 30 points in each direction. The spectrum analyzer records the channel power picked up by the receiving dipole antenna. Channel power is calculated via the integration band width method in which the frequency

detected is swept and an average of the power levels detected taken over the range of frequencies included in the measurement [23].

Repeatability was verified, as shown in Figure 13, by running two tests for the same antenna and frequency and taking the difference of the power results. These two tests were separated in time by running tests of other frequencies for the same antenna before returning to the original frequency and running the test again. As can be seen in the histograms in Figure 13, the range of the data measured at the probe was from 0 to 1.5 mW, and the difference between the measurements ranged from -0.5 to 0.5  $\mu$ W. The histograms on the right represent the number of pixels with a given value corresponding to the plot on the left that has been normalized to each plot's maximum value, so the variance in the data may be seen clearly. The small difference between the two measurements indicates that the measurements from this system are highly repeatable. The antenna's electric field profile was measured for several different frequencies; these results are presented in Chapter 5. Error bars representing the 0.5  $\mu$ W noise are shown on the measured Spatially Averaged Electric Field data plots.

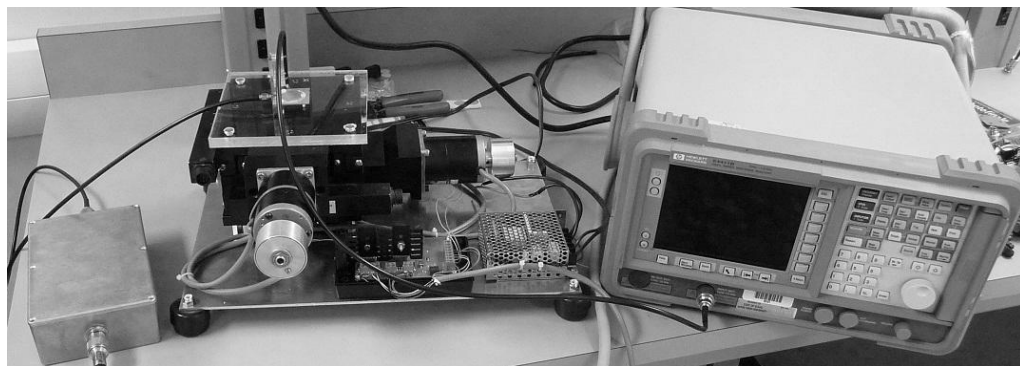


**Figure 11. Photograph of the Electric Field Measurement setup, showing the spectrum analyzer and XY stage.**

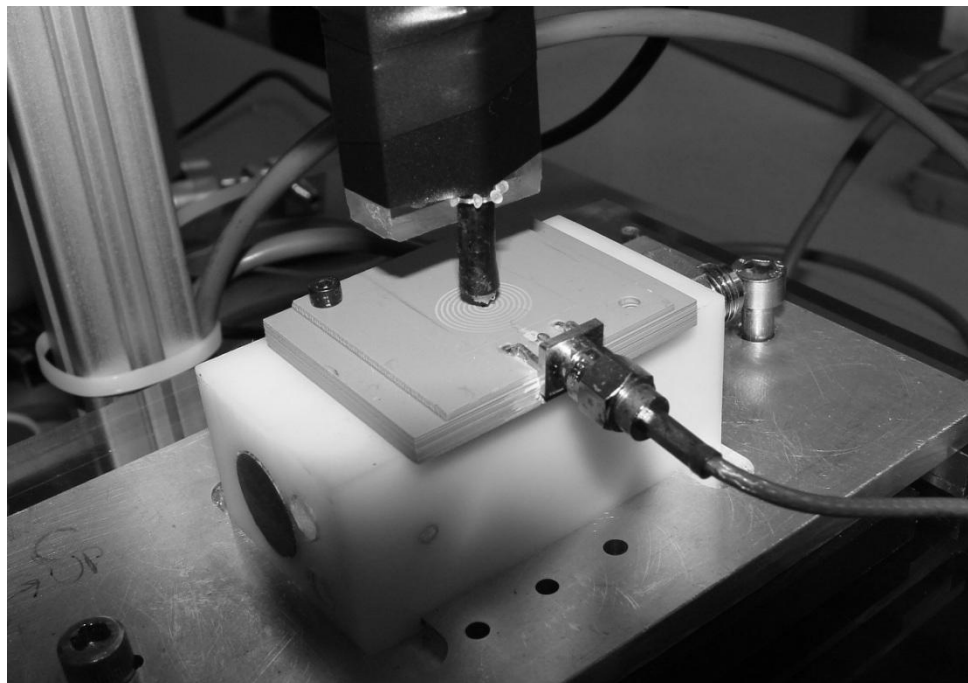


**Figure 12. Photograph of antenna mounted to the Teflon block on the XY stage, showing the RF connection and the dipole antenna probe centered above the antenna, perpendicular to the antenna surface.**

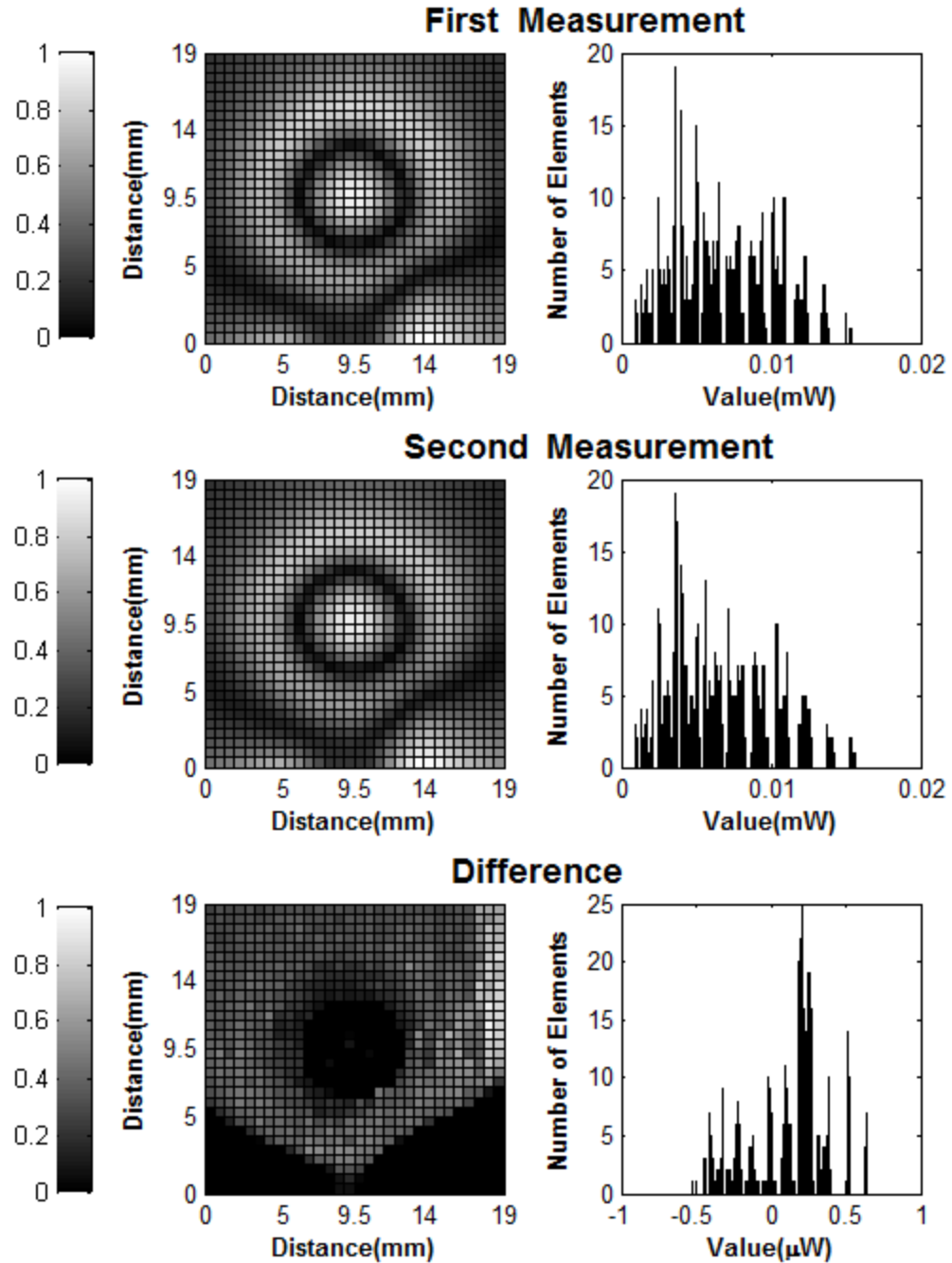


**Figure 13. Repeatability analysis of XY stage measurements. Top: electric field measurement of an antenna, Middle: repeated electric field measurement of an antenna, Bottom: the difference between the two measurements. Left: false color plots showing each data point taken, Right: histograms of the data.**

#### 4.4 Plasma Start Power Measurement

The argon plasma start power was characterized for each antenna. This characterization meant measuring the start powers for the plasma as a function of frequency and argon gas pressure. Figure 14 shows the antenna with an argon plasma. The Teflon block can be seen beneath the LTCC antenna, and the argon connection can be seen on the right. The RF connection is behind the plasma. The plasma thruster group set up these systems and ran the plasma characterization test.

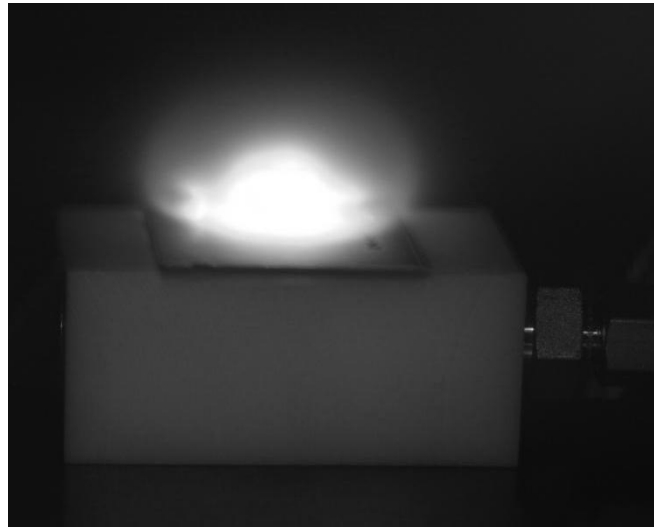


**Figure 14. Photograph of an ICP discharge showing LTCC antenna structure on a Teflon stand with gas inlet connection.**

The plasma start power was measured by placing the antenna in the vacuum chamber and applying increasing power to the antenna until either the plasma initiated or a maximum of 50 W was reached. These measurements were taken for various pressures ranging from 10 mTorr to 1 Torr, with no argon flow to the chamber. At the point at which the plasma initiated, the reflected power from the system would increase. This reflected power data was recorded vs. applied power using the LabView virtual interface,

so the power that the plasma started at was recorded, and the results are shown in Chapter 5.

## CHAPTER 5: RESULTS, COMPARISON AND ANALYSIS

The experimental data and simulated results were compared by using contour plots of the RF fields and by using plots of the average RF field vs. RF frequency. For the contour plots, both experimental and simulated values were imported into MATLAB. The experimental data is imported as a power value in dBm, so this value was converted to mW and then the square root was taken to make the data directly comparable to the simulated electric field data. MATLAB's **contourf** function was then used to create contour plots of both experimental data and simulated results. This method of analysis allows for improved comparison, as distinct levels of intensity can be compared from one result to another. The experimental data and simulation results were spatially averaged as described by Eq. 10 for each operating frequency. In addition, the RF fields were then normalized to the highest value of the field to obtain the relative electric field amplitude. In the case of the XY stage data, N=30 and each pixel is averaged together to determine the average electric field intensity. The electric field probe was not calibrated.

$$E_{avg} = \frac{\sum_{i=1}^N \sum_{j=1}^N \bar{E}_{ij}}{N^2} \quad (\text{Eq. 10})$$

N= number of elements in each direction of array

i,j= indices in each direction of array

$\bar{E}$  = normalized electric field amplitude



The antenna initiates at lower input powers at frequencies for which the electric field intensity is higher for a set input power. Because of this relationship, the square root of the start power (in watts) was taken in order to make the electric field intensity and start power directly comparable. Next, each start power value was inverted so that the highest start power resulted in the lowest value, and the lowest start power resulted in the highest value. Finally, this data was normalized to the highest field value. This analysis makes the start power data directly comparable to the spatially averaged electric field values.

At the beginning of this project, antenna  $\alpha$  was found to initiate plasma. The start power data was taken for a range of frequencies. Next, electric field intensity measurements on the XY stage were taken of the antenna at various frequencies to determine how the field pattern correlated to the start power data. If the antenna provides a high RF field for a given input power frequency, the required input power to initiate plasma is lower. The inverted plasma start power vs. the spatially averaged measured RF electric field intensity is shown in Figure 15. For this comparison, the measured RF electric field was not converted from channel power, and the plasma start power was inverted to show the trend. Both sets of data were normalized to the best-performing case (near 900 MHz).

The results of the plasma start power match the intensity of the electric field power with the exception of a large required plasma start power at 630 MHz that did not appear in the electric field measurement. This difference is assumed to be an effect of the plasma in the chamber and not from the antenna, because the simulated electric field

analysis also did not show the large change at 630 MHz, as is shown in Figure 17 in Section 5.2.

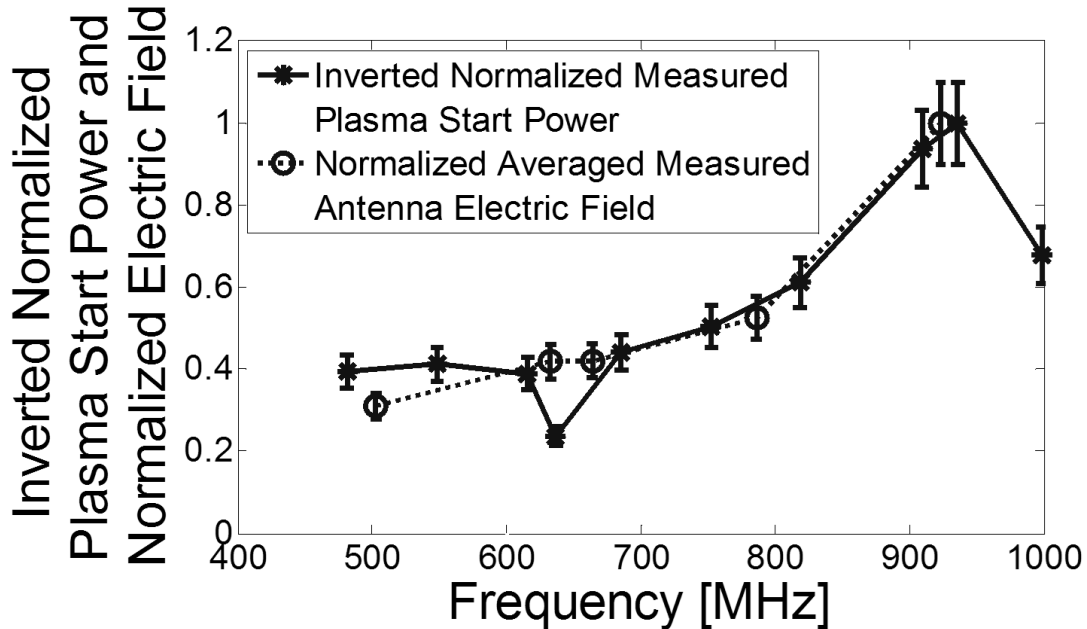


**Figure 15. Inverted, normalized plasma start power at 500 mTorr and normalized, spatially averaged, measured, antenna electric field for antenna  $\alpha$ .**

### 5.1 Simple Antenna Field Calculation

The analysis of the near-field radiation patterns using simple circular loop antennas was plotted vs. frequency for a design with loop radii that match the beginning of each spiral turn in antenna  $\alpha$ , per the process described in Section 3.1.2. The applied signal wavelength comparable to the total conductor length (the wavelength ratio,  $\lambda$ ) was varied from 0.1 wavelengths on total conductor length to one full wavelength on the total conductor length. Because this model uses the wavelengths directly for calculations, varying the frequencies applied and analyzing the permittivity of the material to calculate

the wavelengths was not necessary. The radii values used were 1.25 mm, 2.15 mm, 3.05 mm, 3.95 mm, and 4.85 mm, which the code normalized to the appropriate ratios. Since the code considers the fractions of a wavelength the total conductor covers, only wavelength ratios ( $\lambda$ ) were used for the radii. Figure 16 shows the electric field strength vs. wavelength ratio. The field strength increases from the case in which one tenth of the applied wavelength is covered on the antenna to a maximum where three-fifths of the applied wavelength is equivalent to the total conductor length in the loops. The electric field intensity then decreases until one full wavelength is covered by the total conductor length. This simulation shows that theoretically, the near-field electric field intensity will vary with the frequency applied and that it will behave optimally at roughly 0.65 times the total length of conductor for the approximation where the spiral consists of evenly spaced loops. The dielectric constant of the material results in an RF wavelength on the order of the spiral length. This large ratio greatly affects the field pattern. For antenna  $\alpha$ , the total spiral conductor length is 11 cm. The peak operating frequency is near 900 MHz. By applying the equation to calculate the wavelength of a 900 MHz signal in LTCC (Eq. 11), it was found that the applied wavelength ( $\lambda_{\text{applied}}$ ) was greater than 11.9 cm. The applied wavelength is greater than 11.9 cm because the effective permittivity on the antenna is not quite that of LTCC, as the LTCC only thinly covers the surface of the antenna.

$$\lambda_{\text{applied}} = \frac{1}{f\sqrt{\epsilon_{\text{eff}}\epsilon_0\mu_0}} \quad (\text{Eq. 11})$$

$f$  = frequency (900 MHz)

$\epsilon_{eff}$  = effective permittivity (<7.8)

$\epsilon_0$  = permittivity of free space ( $8.854 \cdot 10^{-12}$  F/m)

$\mu_0$  = permeability of free space ( $4\pi \cdot 10^{-7}$  H/m)

By taking  $\lambda_{\text{applied}} * \lambda = 11.9 \text{ cm} * 0.65 = 7.7 \text{ cm}$ , the ideal spiral would have a total spiral conductor length of greater than 7.7 cm. Since antenna  $\alpha$  has a total spiral conductor length of 11 cm, the antenna  $\alpha$  spiral conductor length is satisfactory for this analysis. Therefore, the interference patterns caused by the different loops in the spiral may be the cause of the variation in performance vs. frequency for antenna  $\alpha$ .

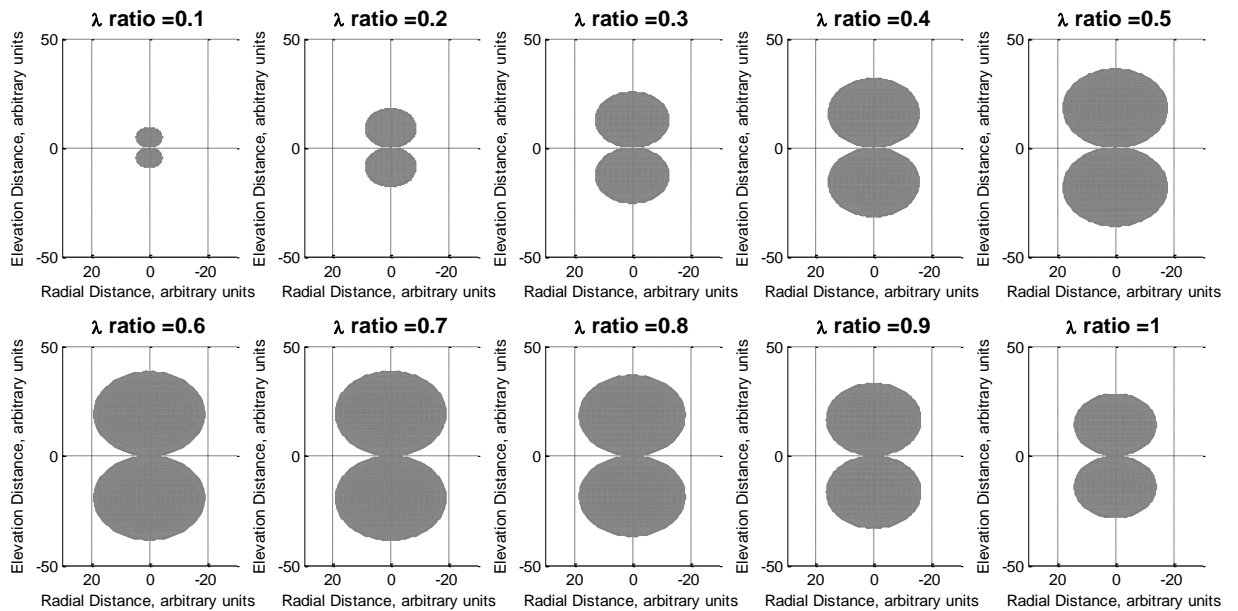


**Figure 16. Field radiation pattern result of the phase-shifted loop approximation of the spiral antenna.**

## 5.2 COMSOL Simulation

### 5.1.1 Model Verification

The comparison of the antenna  $\alpha$  electric field measurement to the COMSOL electric and magnetic field simulation results for several frequencies is shown in Figure 17. The figure is normalized to the peak value, which for antenna  $\alpha$  is the simulated 870 MHz case. The highest measured data value is normalized to match the simulated value at that frequency (923 MHz). The results of the COMSOL simulation match relatively well with the measured values, except for a large peak at 870 MHz. It was not possible to re-measure the electric field data for additional frequencies between 850-900 MHz because the antenna was cracked. However, the plasma start data from Figure 16 shows the lowest start powers between 900 MHz and 923 MHz, suggesting that the electric field maximum is in that range. This difference between the measured and simulated electric fields is thought to be due to variations in the fabrication process. The simulated electric and magnetic fields were also a good match, showing that the simulated electric field intensity is a good indicator of the magnetic field in the device, and thus a good indicator of the performance of the antenna.

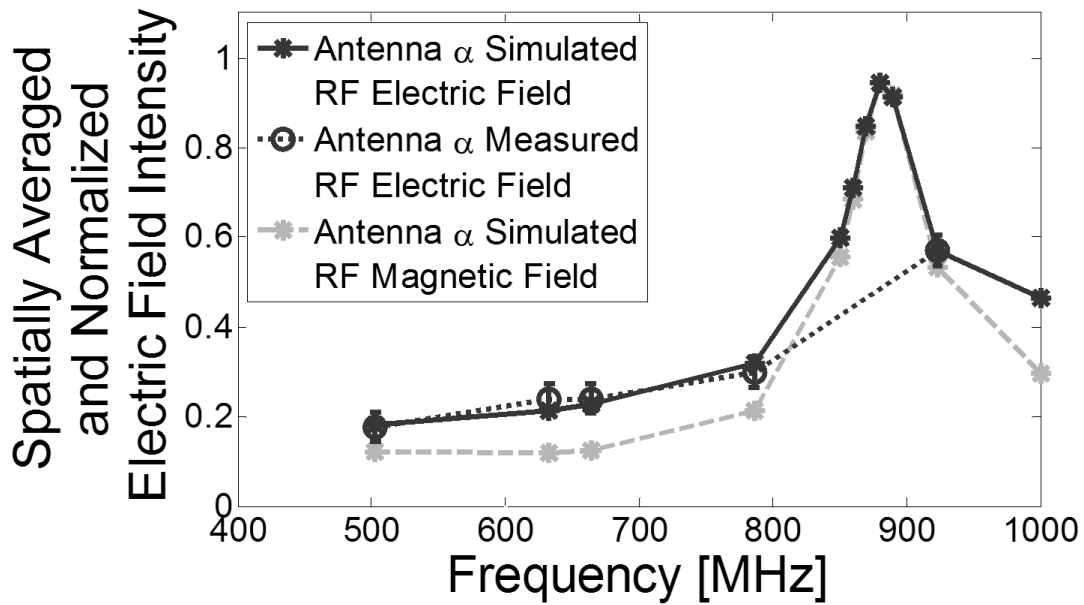


**Figure 17. Measured and simulated electric field intensity ratios for antenna  $\alpha$ , normalized to the 923 MHz case.**

### 5.1.2 Design Parameter Analysis

Once the antenna model was verified, the next step was to determine what design factors most influenced the antenna's performance. These parameters included dielectric permittivity, depth of conductor in LTCC, trace width, trace pitch, number of turns, total conductor length, and depth of electrical via. Many of these parameters are related. The total conductor length is influenced by the pitch and number of turns. All of the parameters influence the inductance/capacitance of the antenna.

The first thing to determine was whether or not the high permittivity of the LTCC was causing the variation in performance vs. frequency (as in Figures 16 and 17). To simulate this effect, the wave equation used for LTCC was replaced with the wave equation for air in COMSOL. The results are shown in Figure 18 for both  $\epsilon_r=7.8$  and

$\epsilon_r=1.0$ . It was found that there was essentially no change in the RF field vs. frequency of the antenna in air, so the high permittivity of LTCC was causing the strong variation in average electric field intensity vs. frequency. In fact, if the air simulation was continued up to 2 GHz, similar peaks to the LTCC simulation appeared. In both cases the peak occurred in the region where the wavelength of the applied frequency in the material became similar to the total length of conductor in the antenna. This result indicates that the length of the conductor vs. the wavelength of the applied frequency is the cause of the peak in the RF field.

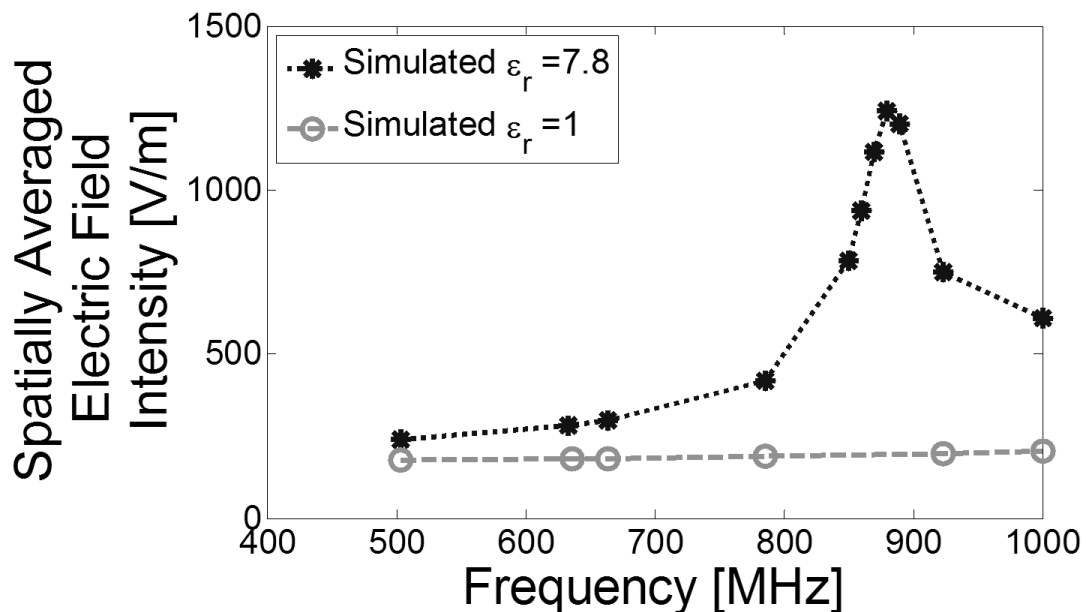


**Figure 18. Simulated electric field intensity for antenna in LTCC ( $\epsilon_r=7.8$ ) and in air ( $\epsilon_r=1$ ).**

Next, other parameters were analyzed. By increasing the electrical via depth from 0.14 mm to 0.94 mm, it was found that the frequency where the simulated maximum in average electric field intensity occurred (peak frequency) shifted to a higher frequency, as

shown in Figure 19. This could be due to the fact that the capacitance between the coil and the connecting trace that travels below the coil is decreased, which would shift a resonance frequency to a higher value. If the trace width was increased instead from 0.36 mm to 1.08 mm, the peak frequency shifted to a lower value, as shown in Figure 20. This shift in peak frequency corresponds to the idea that there are some resonant frequency effects contributing to the peak. In both cases the intensity of the peak was diminished. The antenna could only be embedded in the LTCC 1 layer deep (35  $\mu\text{m}$  post-firing), so the antenna could be embedded no less than the thickness of the thinnest sheet of LTCC. More than 1 layer deep was undesirable because it decreased the peak field that would interact with the plasma. The direct write tool is set up such that it is unable to reliably fabricate devices with a pitch of less than 0.7 mm. It can only make conductor trace widths at set values. The width of 0.36  $\mu\text{m}$ , which was used for the original antenna, was the narrowest obtainable value [16]. The depth of the electrical via for the antenna also had to be a multiple of the thickness of the LTCC sheets and could not exceed the depth of the LTCC substrate that contained the antenna. The design constraints prevent fabricating a device with a smaller electrical via depth or a narrower trace width, so these values were kept constant for future simulations.



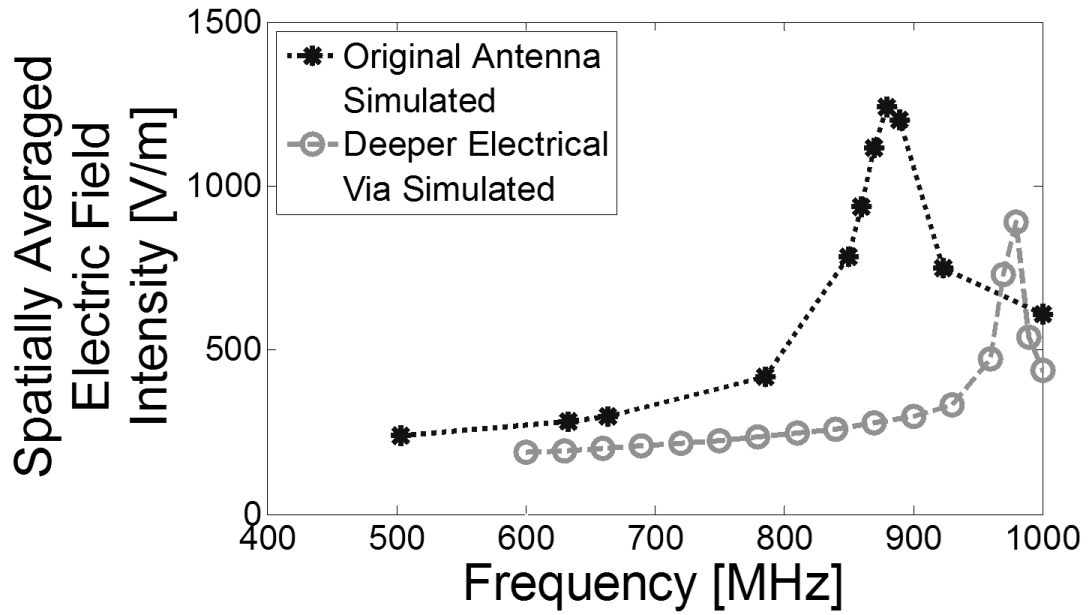


Figure 19. Simulated average electric field intensity vs. frequency for antenna  $\alpha$  design and for a deeper electrical via.

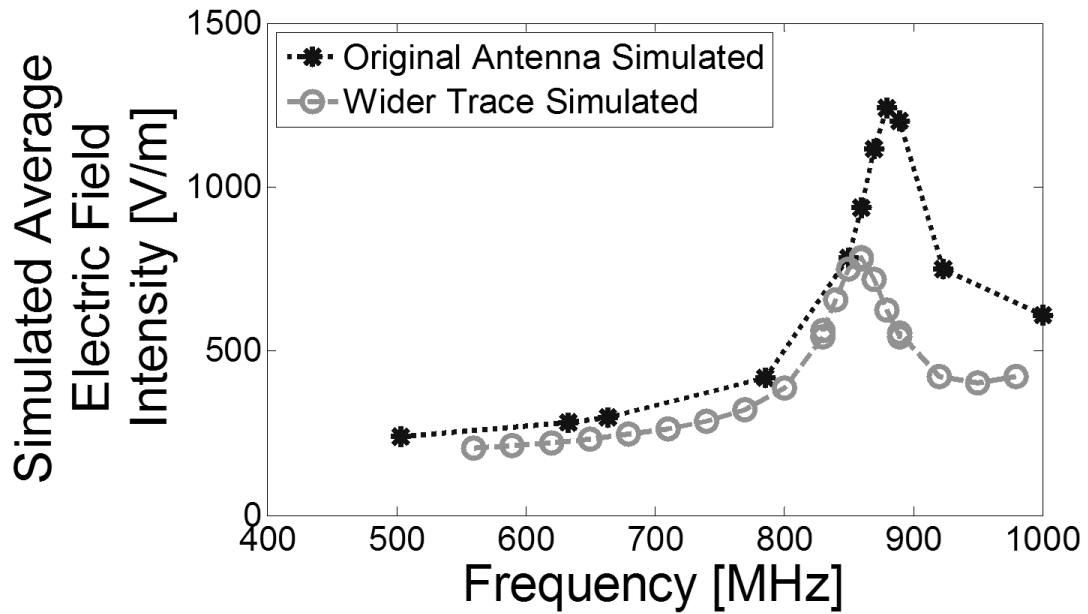
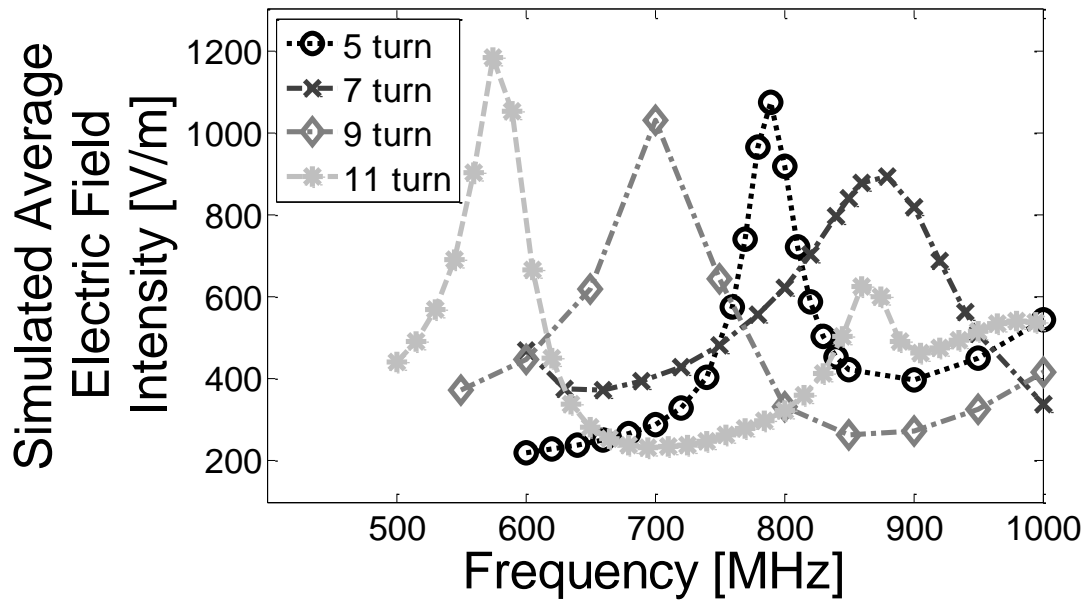


Figure 20. Simulated average electric field intensity vs. frequency for antenna  $\alpha$ , and for a wider conductor trace.

### 5.1.3 New Antenna Designs

Once the via depth and trace width design parameters were analyzed, a second set of simulations were run in order to look for improvements to the design. The tests were run for 4 antenna designs all with the original antenna trace width, antenna depth, and electrical via depth. The antennas had 5, 7, 9, and 11 turns. Each antenna's pitch was set such that the distance from the center of the antenna to the outermost point on the spiral was near 7.5 mm; this value was chosen to give an antenna diameter of near 15 mm, which fits nicely underneath the intended 2 cm diameter thruster body. The spatially averaged, normalized fields are plotted vs. frequency, and the simulation results are shown in Figure 21. The highest field peak occurred at 575 MHz for the 11 turn antenna; however, that frequency is below the desired operating frequency range. Higher frequencies are more desirable because they create plasmas with a smaller skin depth and higher field penetration than the lower frequencies. The 5 turn and 9 turn antenna each had reasonably high peaks as well (at 790 MHz and 700 MHz, respectively), so these two were selected for fabrication. The 7 turn antenna had a peak at 880 MHz, but the magnitude of the peak was lower than that of the other antennas. The peaks were comparable in average electric field intensity when compared vs. antenna diameter; however, the newer antenna designs are of a larger diameter. Because the 9 turn antenna has a small pitch, the center turn was removed (making it an 8 turn antenna) to make room for a gas inlet.



**Figure 21. Simulated average electric field intensity vs. frequency for 5, 7, 9, and 11 turn antennas, all with an outer diameter of approximately 15mm.**

After fabrication of the two antennas, the antenna fields were measured on the XY stage. It was found that some features of the antennas were not as designed due to fabrication adjustments. So the antennas were re-simulated with the actual fabrication dimensions. The fabricated 8 turn, 15 mm antenna is called antenna  $\beta$ , and the fabricated 5 turn, 15 mm antenna is called antenna  $\gamma$ . The simulation results for antenna  $\gamma$  roughly matched the electric field measurement data as is shown in Figure 22. There is a peak near 730 MHz in both cases, but the simulated data shows the field intensity diminishing more quickly as the frequency changes. This wider frequency range at which the antenna's electric field intensity is high is similar to the comparison from measured to simulated electric field for antenna  $\alpha$ . The different shapes of the peaks are most likely due to irregularities in the conductor trace width from fabrication.

The simulation results for antenna  $\beta$  also roughly match the electric field measurement with an interesting new characteristic appearing for antenna  $\beta$ : two peaks over the analyzed frequency range. The two peaks occur near 757 MHz and 469 MHz, as shown in Figure 23. A peak near 805 MHz was expected, but the 469 MHz peak was not. More simulations were done to include the lower frequencies. A simulated peak at 505 MHz was found. The 469 MHz peak is believed to be caused by the ratio of the separation between the coil and the ground trace beneath the coil vs. the separation of the turns in the antenna. This effect is described in Section 5.1.4. The measured and simulated data both show peaks near the expected range, with a few interesting differences. The simulated results show a peak with a wider frequency range that is centered at a lower frequency than the measured peak at 805 MHz. This difference could be due to a narrower trace width than what was simulated, as well as other fabrication effects. The measured peak at 469 MHz instead of 505 MHz could be caused by this as well. To confirm this, another cross-section measurement of the antenna as fabricated would need to be made.

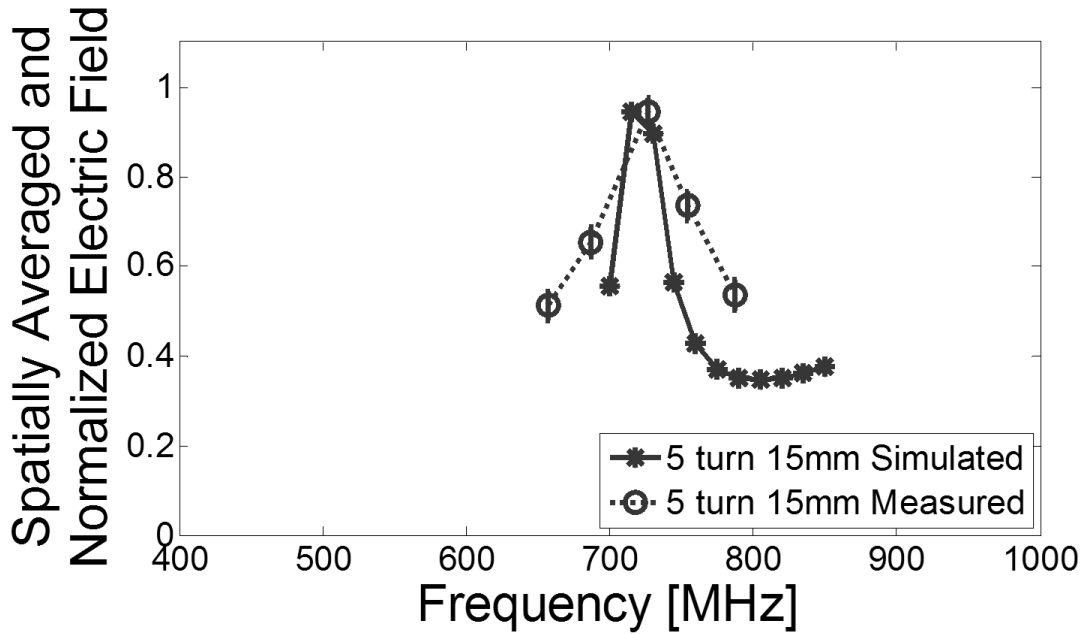


Figure 22. Measured and simulated electric field intensity ratios for antenna  $\gamma$ , measured data is normalized to the 727 MHz case, simulated data is normalized to the 730 MHz case.

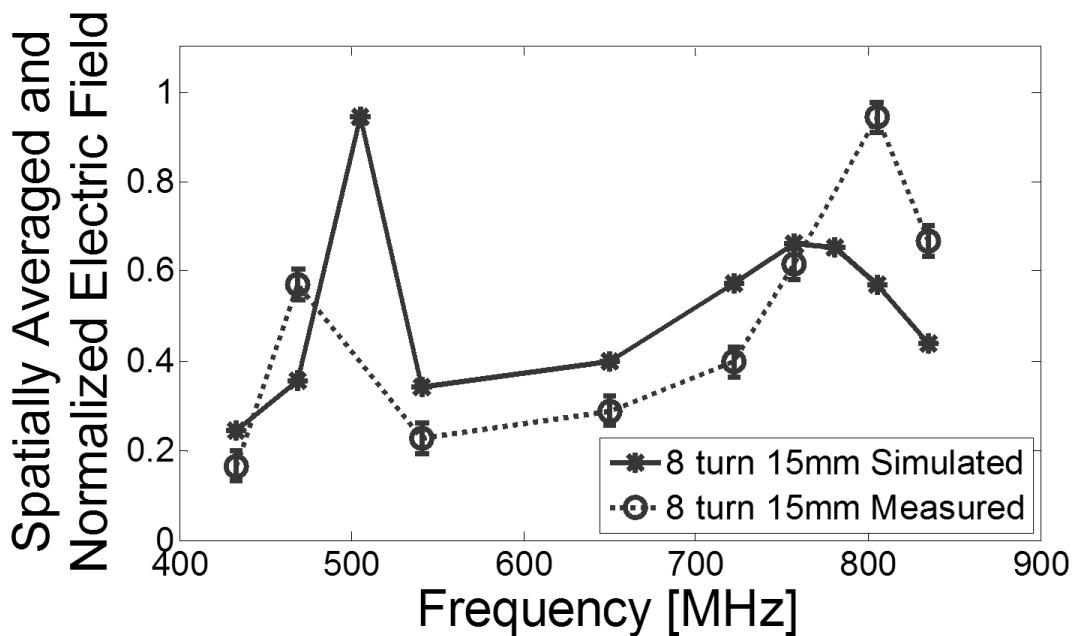


Figure 23. Measured and simulated electric field intensity ratios for antenna  $\beta$ , measured data is normalized to the 805 MHz case, simulated data is normalized to the 500 MHz case.

The experimental data was also plotted as normalized contour plots. These plots all show a ring of high electric field intensity at the antenna's ideal operating frequency. These results are shown in Figures 24-29 for a range of frequencies and antennas. The differences between the experimental and simulated results can be explained by the imperfections in the trace width from fabrication.

Antenna  $\alpha$  measured electric field intensity contour plots are in Figure 24. The maximum field is at 923 MHz, and each contour plot has a similar arc shape on the left of the plot. This arc shape follows along the spiral shape, with growing intensity as the frequency increases. The arc does not form a complete circle because the field is lower in the region where the cable connects to the antenna (at the bottom center of each plot) and also where the bottom trace crosses beneath the coil. In the simulated plot (Figure 25) the arc shape is less pronounced, and the contours form a more complete ring, slightly farther in towards the center of the antenna than the measured data. In the simulated results the highest performing frequency is 880 MHz. The electric field measurement data does not include 880 MHz, as the peak in the start power data taken was very near 923 MHz and began to decline at 900 MHz.

Antenna  $\beta$  measured electric field intensity contour plots are in Figure 26. The maximum field is at 805 MHz; these contours are smaller ring shapes from roughly 6 mm to 13 mm on the plots. The simulation contour plots in Figure 27 are of a similar shape, but the maximum field is between 805 MHz and 757 MHz, and the ring shapes extend from roughly 4 mm to 15 mm.

Antenna  $\gamma$  measured electric field intensity contour plots are shown in Figure 28. Again, the data contours primarily form ring shapes with the maximum field occurring at 727 MHz. The simulated contours in Figure 29 are primarily more arc shaped with the maximum field at 730 MHz. The simulated fields also show more effects from the connector and bottom trace than the measured electric field data.

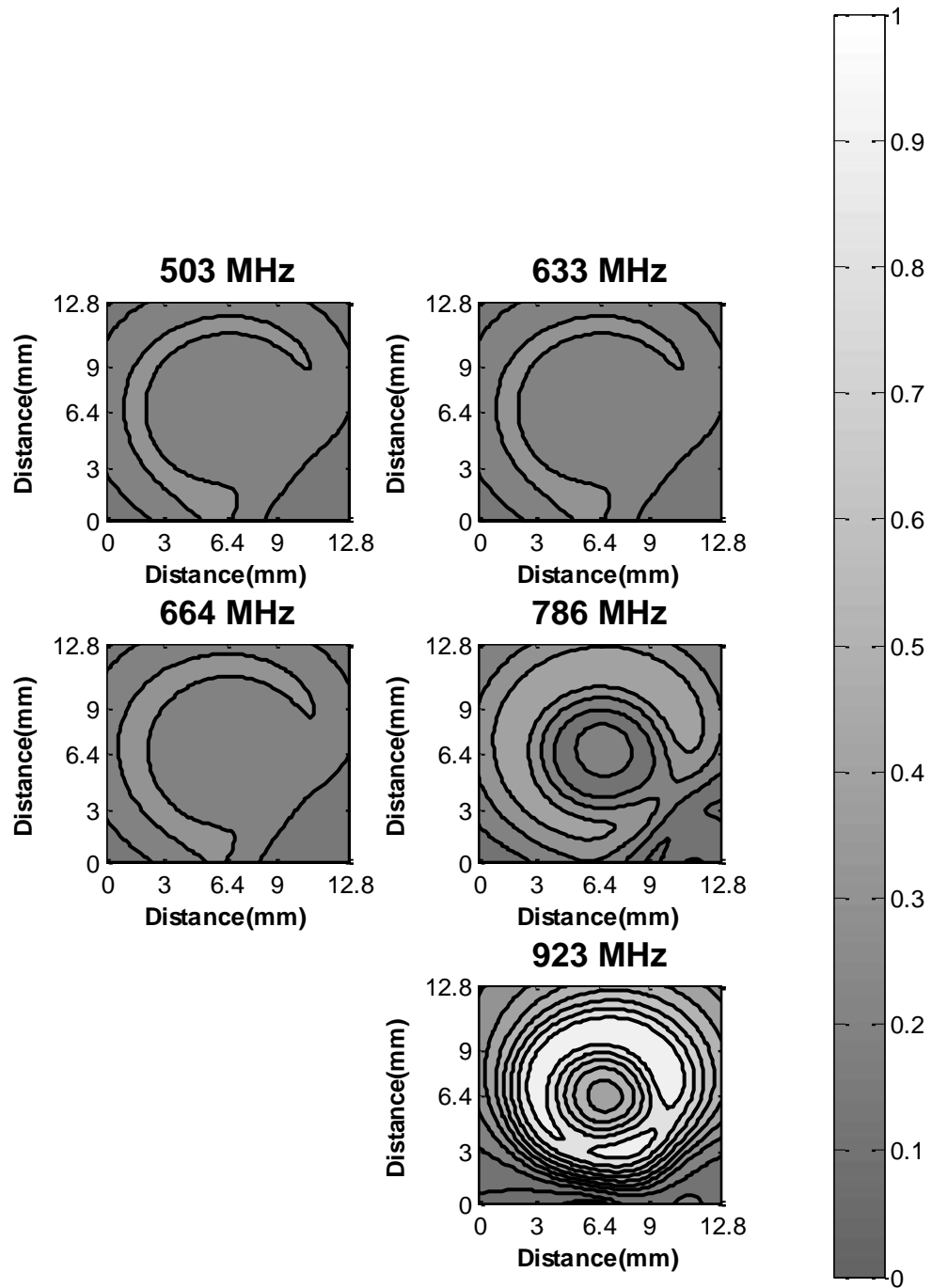


Figure 24. Contours of experimentally measured electric field intensity for antenna  $\alpha$ , normalized to the 923 MHz case.



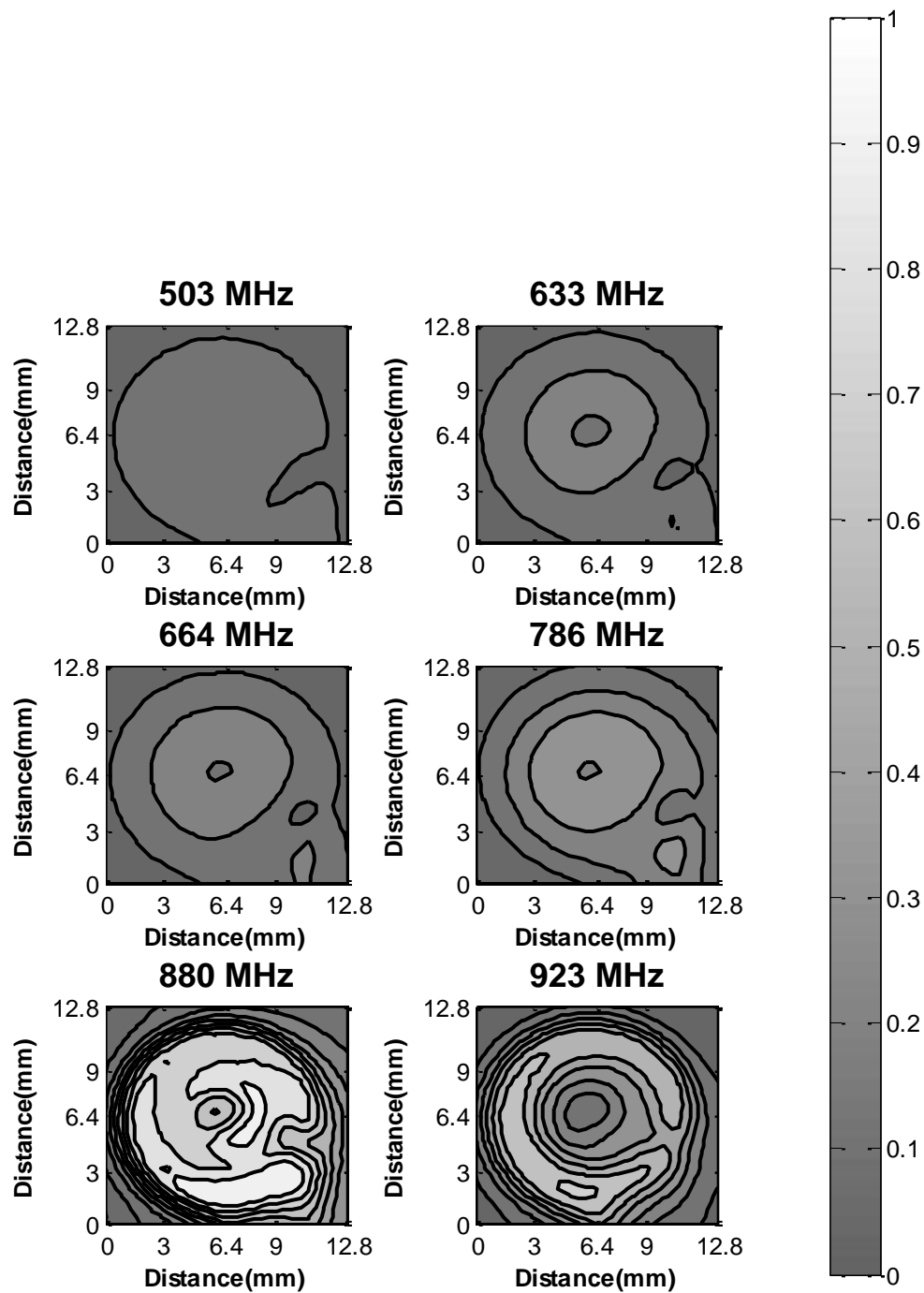


Figure 25. Contours of simulated electric field intensity for antenna  $\alpha$ , normalized to the 923 MHz case.

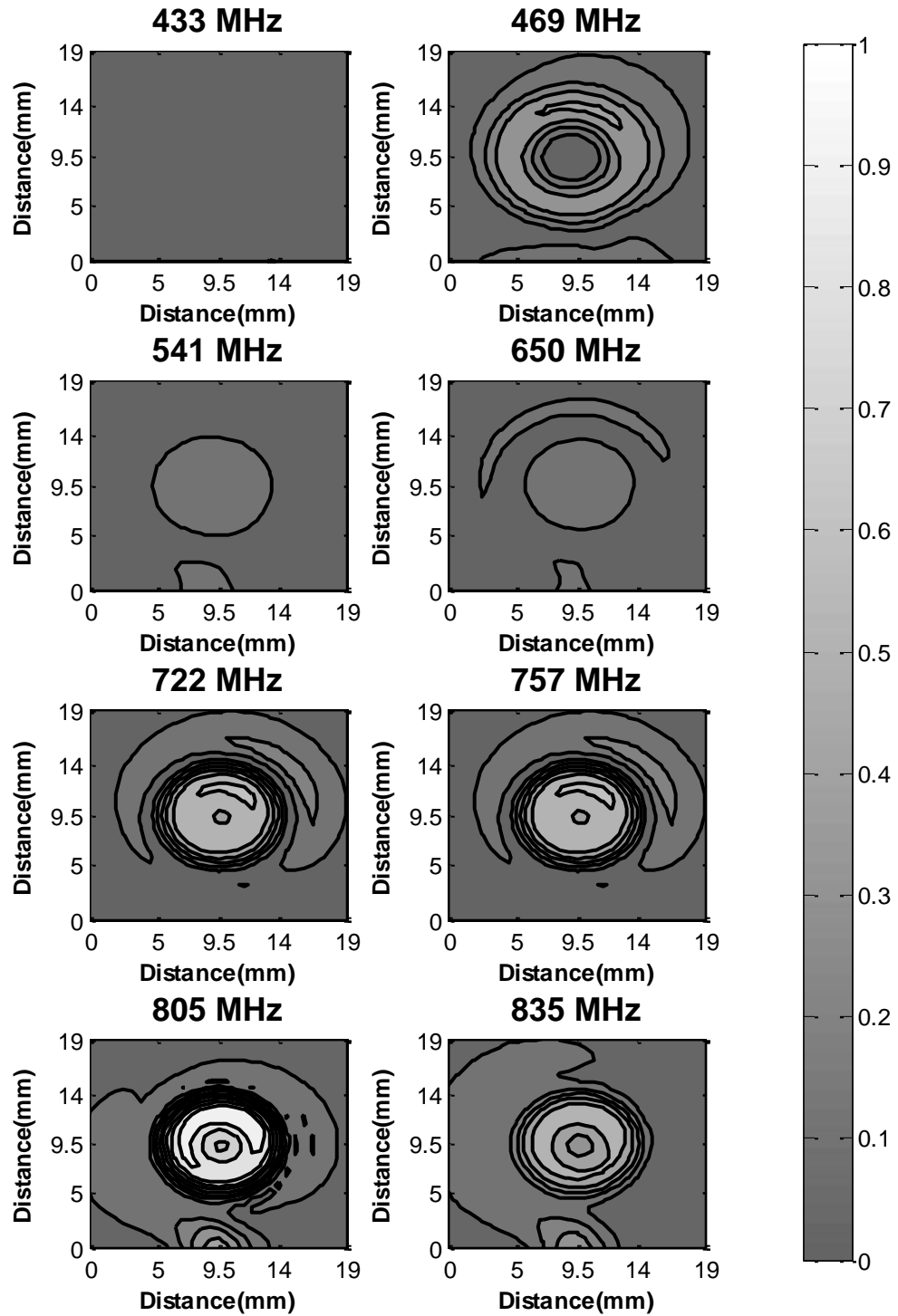


Figure 26. Contours of experimentally measured electric field intensity for antenna  $\beta$ , normalized to the 757 MHz case.

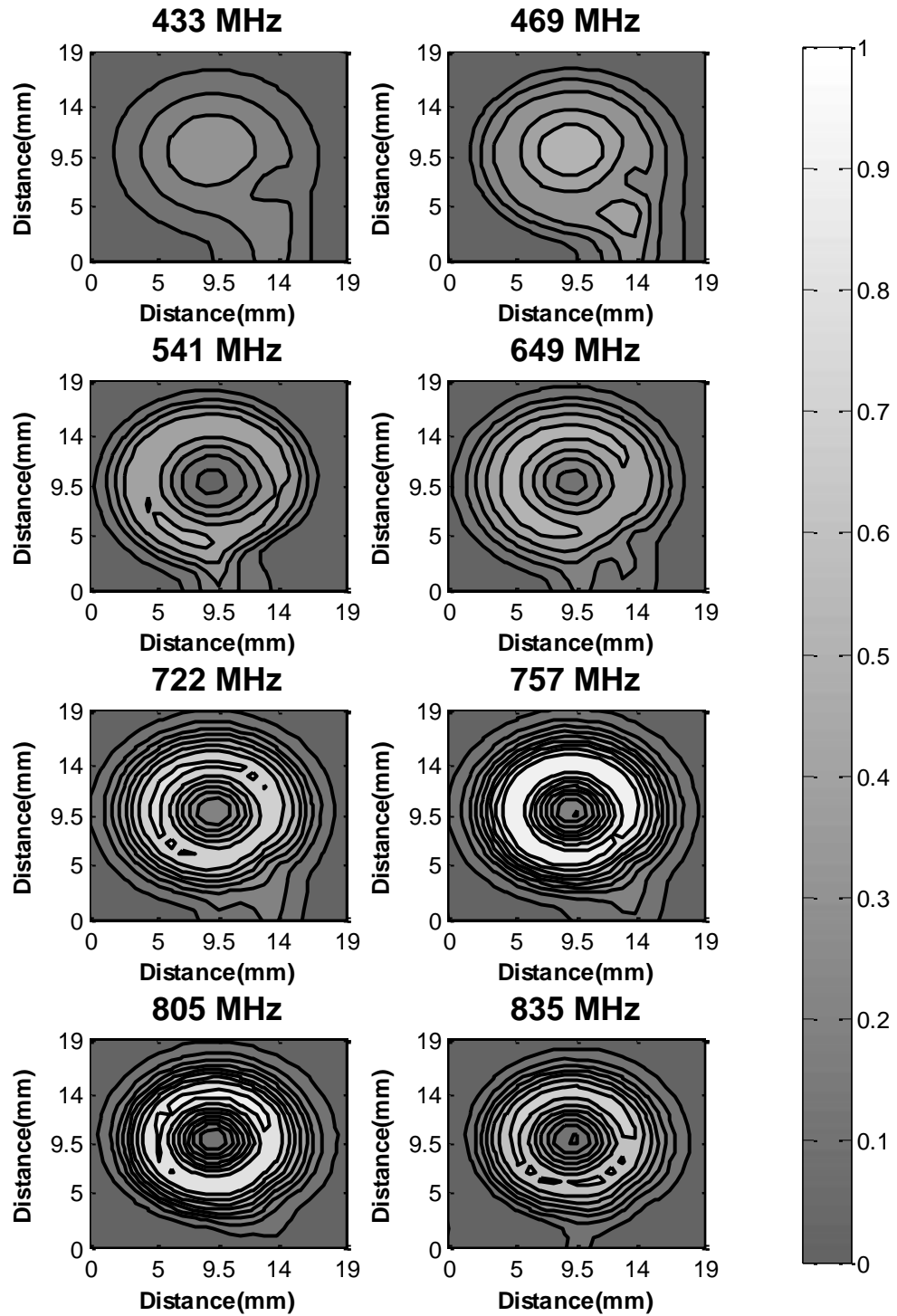
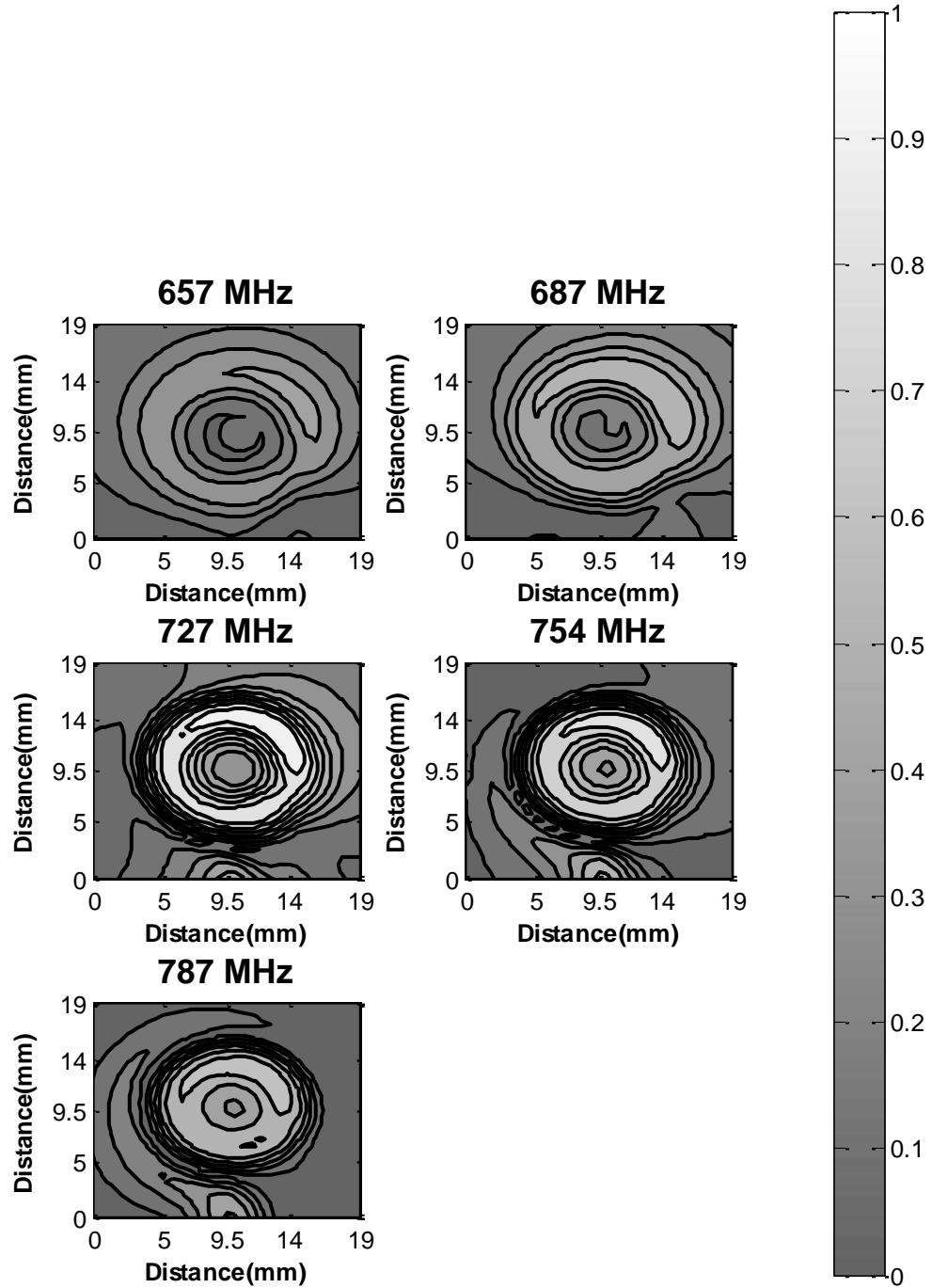
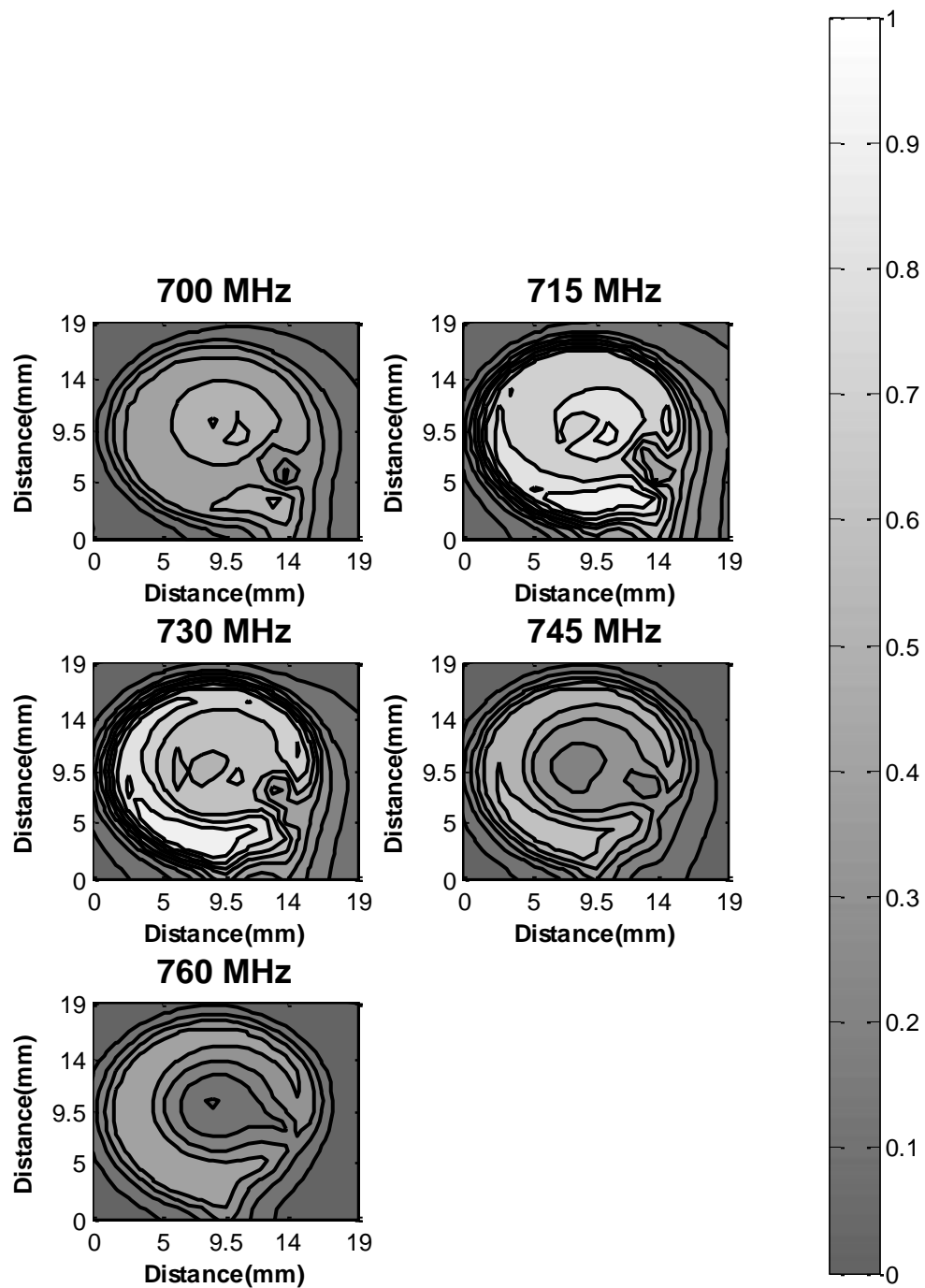


Figure 27. Contours of the simulated electric field intensity for antenna  $\beta$ , normalized to the 757 MHz case.



**Figure 28.** Contours of experimentally measured electric field intensity for antenna  $\gamma$ , normalized to the 727 MHz case.



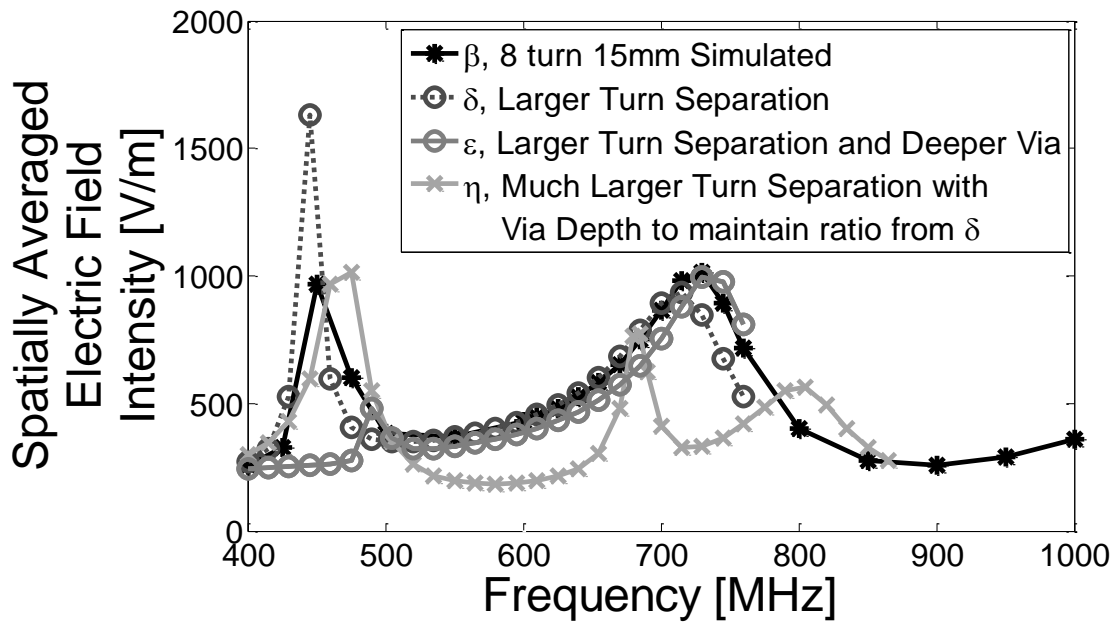
**Figure 29.** Contours of simulated electric field intensity for antenna  $\gamma$ , normalized to the 730 MHz case.

#### 5.1.4 Analyzing Behavior of Low-Frequency Peak

The second, lower frequency peak for antenna  $\beta$  was unexpected when the initial designs were established. So an attempt was made to understand the behavior of this peak. A check was done for frequencies from 300 MHz to 700 MHz in the simulation in antenna  $\gamma$ , and no other peaks were found. For the purpose of characterizing the behavior of the low-frequency peak in antenna  $\beta$ , a COMSOL simulation was run wherein the maximum width of the trace was increased to 0.45 mm and the pitch was decreased to 0.726 mm, resulting in a trace separation distance of 0.276 mm (called antenna  $\delta$ ). It is not possible to fabricate this device, but simulating it gave a better idea of why the peak occurred. A summary of the antennas that were simulated for the low-frequency peak analysis is in Table 1, and a plot of the spatially averaged simulated electric fields is shown in Figure 30. This simulation of antenna  $\delta$  showed the intensity of this peak nearly doubled while the frequency shifted lower very slightly. Next, the depth of the via was increased; this case (called antenna  $\epsilon$ ) gave a significantly diminished peak intensity at a slightly higher frequency. The simulated higher frequency peak remained relatively unaffected by these geometry changes. Finally, a simulation (called antenna  $\eta$ ) was run that roughly quadrupled both the trace separation distance and via depth of antenna  $\epsilon$ . To get these values, the width of the trace was returned to 0.36 mm, and the pitch was increased to 1.48 mm. This geometry, called antenna  $\eta$ , successfully simulated a peak at the lower frequency value. Because this geometry had such a large pitch, the total conductor length in the spiral was increased from 21 cm to 36 cm, and thus the higher frequency peak shifted to a lower frequency value (from near 757 MHz to near 680 MHz).

**Table 1: List of antennas analyzed for the lower-frequency peak**

	Trace Separation Distance (mm)	Via Depth (mm)
$\beta$	0.42	0.14
$\delta$	0.276	0.14
$\epsilon$	0.276	0.54
$\eta$	1.12	0.56

**Figure 30. Comparison of simulated average electric field intensities for antennas  $\beta$ ,  $\delta$ ,  $\epsilon$ , and  $\eta$ , not normalized.**

#### 5.1.4 Simulation Performance Comparison of Antennas $\alpha$ , $\beta$ , and $\gamma$

After the antennas had been fabricated, tested, and the simulations adjusted so that the experimental electric field measurements could be compared to the simulation, the final fabricated geometries as simulated in COMSOL were compared to look for improvement to electric field intensity overall. The results can be seen in Figure 31. As shown in previous figures, antenna  $\alpha$  has an average simulated RF field peak of 1242 V/m at 880 MHz, antenna  $\beta$  has an average simulated RF field peak of 769.6 V/m at 500 MHz, and antenna  $\gamma$  has an average simulated RF field peak of 1154.9 V/m at 730 MHz. Antenna  $\beta$  was not able to reach sufficiently high electric field intensities to be preferable to antenna  $\gamma$ . Neither antenna  $\beta$  nor  $\gamma$  has quite enough electric field intensity at the peak frequency to be preferable to antenna  $\alpha$  if only the diameter across the antenna is considered, rather than similarly sized areas above each antenna. If the thruster body size is considered, however, then antenna  $\gamma$  is the best choice for an operating antenna out of the tested designs, as it provides nearly equivalent electric field intensity to antenna  $\alpha$  with a larger surface area for interactions to occur.



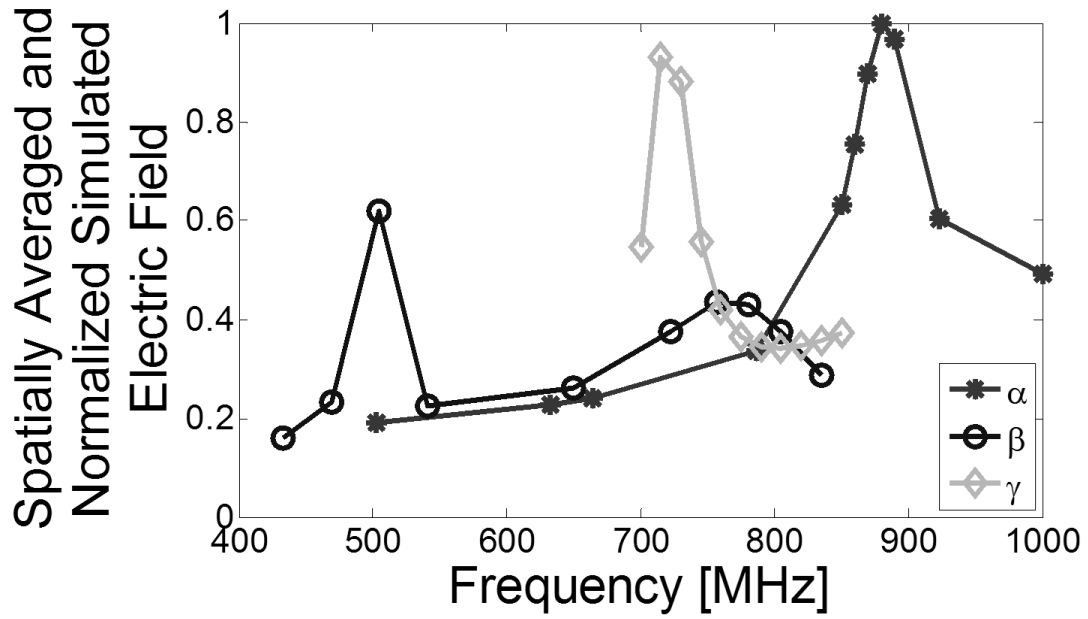


Figure 31. Comparison of simulated average electric field intensities for antennas  $\alpha$ ,  $\beta$ , and  $\gamma$ , normalized to antenna  $\alpha$  923 MHz case.

## CHAPTER 6: CONCLUSIONS AND FUTURE WORK

### 6.1 Conclusions

Successful ICP antenna models were created and used to design an antenna for the thruster design. Numerical performance models were created in both MATLAB and COMSOL. It was found from using MATLAB to perform a simple loop calculation that when the frequency is such that one wavelength is near the total conductor length in the spiral, the performance of the antenna will change. The optimal performance, as approximated by loops instead of a full spiral, occurred when the total conductor length is 0.65 times the applied signal's wavelength. A COMSOL model of the electric field was developed and verified against both experimental electric field measurements and plasma start power measurements. The COMSOL model verified that the LTCC substrate decreases the RF wavelength, causing a strong frequency variation of the fields. If a low-permittivity material is used with the same antenna-coil design, there is very little performance change vs. frequency. Both lower frequency and higher frequency peaks were found and analyzed. It was found that the higher frequency peak could be best manipulated by changing the pitch and number of turns in the antenna. It was found that the lower frequency peak could be best manipulated by changing the ratio of the separation between each turn in the antenna and the depth of the electrical via. Antenna  $\gamma$  (a 5 turn, 15 mm diameter antenna with a 1.45 mm pitch) was determined to be the best design for thruster operation out of the designs analyzed.

## 6.2 Future Work

In future design work, designs with larger pitch and fewer turns such as antenna  $\gamma$  will be more robust. This is because the larger pitch is less influenced by variations in the trace width, and by having fewer turns the total conductor length is less influenced by shrinkage during firing. Alternatively, fabrication methods could be developed to mitigate these variances.

Future work would include changing the number of turns in an attempt to manipulate the frequency that the lower-frequency peak occurs at and would include an attempt to manipulate the frequency of each of the peaks to merge them to obtain a higher electric field intensity than possible with either peak alone. Furthermore, future simulations would use the entire thruster configuration to confirm the behavior of the antenna within the thruster design using start power measurements, as well as compare the experimental start power measurements vs. frequency with simulation results.

## References

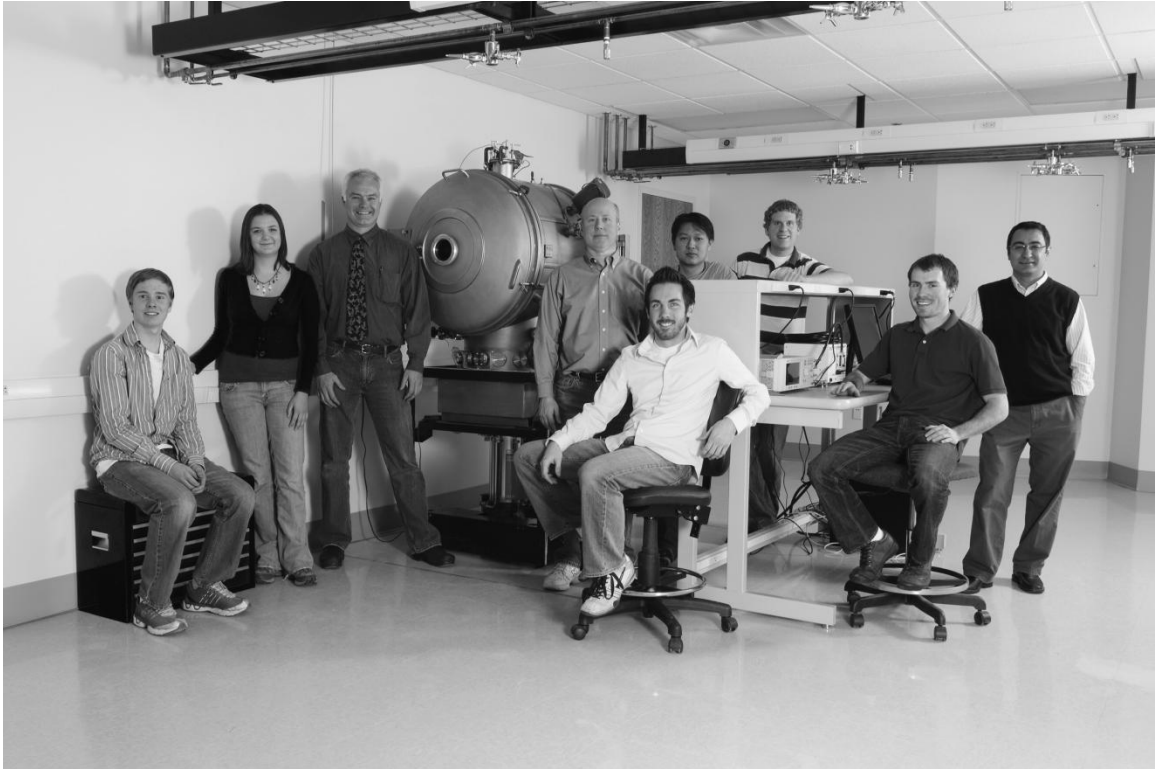
- [1] DuPont 951 Green Tape Product Description. [Online].  
[http://www2.dupont.com/MCM/en\\_US/assets/downloads/prodinfo/951LTCCGreenTape.pdf](http://www2.dupont.com/MCM/en_US/assets/downloads/prodinfo/951LTCCGreenTape.pdf)
- [2] Y. Yin, J. Messier, and J. Hopwood, "Miniaturization of inductively coupled plasma sources," *IEEE Trans. Plasma Sci.*, vol. 27, no. 5, pp. 1516-1524, Oct. 1999.
- [3] J. Mueller, "Thruster Options for Microspacecraft: A Review and Evaluation of State-of-the-Art and Emerging Technologies," in *Micropropulsion for Small Spacecraft*, Inc. Charles Stark Draper Laboratory, Ed. Pasadena, CA: American Institute of Aeronautics and Astronautics, Inc., 2000, ch. 3, pp. 45-137.
- [4] D. Goebel, I. Katz, *Fundamentals of Electric Propulsion: Ion and Hall Thrusters.*: JPL Space Science and Technology Series, 2008.
- [5] S. Liao, *Microwave Electron-Tube Devices*. Englewood Cliffs, New Jersey: Prentice-Hall, Inc., 1988.
- [6] M. Lieberman and A. Lichtenberg, *Principles of Plasma Discharges and Materials Processing.*: John Wiley & Sons, Inc., 2005.
- [7] M.D. Henry, D.E. Brinza, A.T. Mactutis, A.T. McCarty, J.D. Rademacher, T.R. vanZandt, R. Johnson, S. Moses, G. Musmann, F. Kuhnke, "NSTAR diagnostic package architecture and Deep Space One spacecraft event detection," *Aerospace Conference Proceedings*, vol. 6, pp. 293-307, 2000.

- [8] J.E. Polk, R.Y. Kakuda, J.R. Anderson, J.R. Brophy, V.K. Rawlin, M.J. Patterson, J. Sovey, and J. Hamley, "Validation of the NSTAR ion propulsion system on the deep space one mission: Overview and initial results," in *Joint Propulsion Conf.*, Los Angeles, CA, 1999, pp. AIAA-99-2274.
- [9] D.L. Estublier, "The SMART-1 Spacecraft Potential Investigations," *IEEE Transactions on Plasma Science*, vol. 36, no. 5, pp. 2262-2270, Oct. 2008.
- [10] I.D. Boyd, "Numerical Simulation of Hall Thruster Plasma Plumes in Space," *IEEE Transactions on Plasma Science*, vol. 34, no. 5, pp. 2140-2147, Oct. 2006.
- [11] J. Hopwood, "Planar RF induction plasma coupling efficiency," *Plasma Sources Sci. Technol.*, vol. 3, no. 4, pp. 460-464, Nov. 1994.
- [12] J. Hopwood, O. Minayeva, and Y. Yin, "Fabrication and characterization of a micromachined 5 mm inductively coupled plasma generator," *J. Vac. Sci. Technol. B, Microelectron. Nanometer Struct.*, vol. 18, no. 5, pp. 2446-2451, Sep 2000.
- [13] J. Hopwood, "A microfabricated inductively coupled plasma generator," *J. Microelectromech. Syst.*, vol. 9, no. 3, pp. 309-313, Sep 2000.
- [14] F. Iza and J. Hopwood, "Influence of operating frequency and coupling coefficient on the efficiency of microfabricated inductively coupled plasma sources," *Plasma Sources Sci. Technol.*, vol. 11, no. 3, pp. 229-235, Aug 2002.

- [15] R. Wirz, J. Polk, C. Marrese, J. Mueller, J. Escobedo, P. Sheehan, "Development and Testing of a 3cm Electron Bombardment Micro-Ion Thruster," in *27th Int. Electric Propulsion Conf.*, Pasadena, CA, 2001, pp. IEPC-01-343.
- [16] J. Taff, S. Shawver, M. Yates, C. Lee, J. Browning, D. Plumlee, "Fabrication of an Inductively Coupled Plasma Antenna in Low Temperature Co-Fired Ceramic," *International Journal of Applied Ceramic Technology*, Feb 2012.
- [17] D. Plumlee, J. Steciak, A. Moll, "Development and Simulation of an Embedded Hydrogen Peroxide Catalyst Chamber in Low-Temperature Co-Fired Ceramics," *International Journal of Applied Ceramic Technology*, vol. 4, no. 5, pp. 406-414, 2007.
- [18] [Online]. <http://www.comsol.com/>
- [19] A. Polycarpou, *Introduction to the Finite Element Method in Electromagnetics*, 1st ed., Arizona State University Constantine A. Balanis, Ed. United States of America: Morgan & Claypool, 2006.
- [20] (2012) MATLAB The Language of Technical Computing. [Online]. <http://www.mathworks.com/products/matlab/>
- [21] Constantine A. Balanis, *Antenna Theory Analysis and Design*, 3rd ed. Hoboken, New Jersey: John Wiley & Sons, 2005.
- [22] J. Browning, C. Lee, D. Plumlee, S. Shawver, S. M. Loo, M. Yates, M. McCrink, J. Taff, "A Miniature Inductively Coupled Plasma Source for Ion Thrusters," *IEEE Trans. Plasma Sci.*, vol. 39, no. 11, pp. 3187-3195, Nov. 2011.

- [23] Agilent Technologies. (2008, June) [Online].  
<http://cp.literature.agilent.com/litweb/pdf/E4440-90618.pdf>

## APPENDIX A

**EPROP Research Group**

**Figure A.1. EPROP Research Group. From left to right: Logan Knowles, Sonya Shawver (the author), Don Plumlee, Jim Browning, Matt McCrink, Sin Ming Loo, Carl Lee, Jack Woldtvedt, Inanc Senocak. The vacuum chamber is in between Drs. Plumlee and Browning. Not pictured: Mallory Yates, Peter Bumbarger, Jesse Taff, Derek Reis, Kelci Parrish, Dr. Amy Moll.**



## APPENDIX B

### COMSOL RF Simulation Model Development

The **rf\_coil** tutorial module was used as a guide to create the COMSOL models presented in this thesis. The process followed to create the models is as follows.

#### Initiating Model

When creating a new model, the user is prompted to select the physics type and study type. Models all contain the following sections: **Definitions, Geometry, Materials, Physics, Mesh, Study, and Results**. These options can be seen in Figure B1. Under each section features may be added. To see these options right click while hovering over a section in COMSOL, as shown in Figure B2.

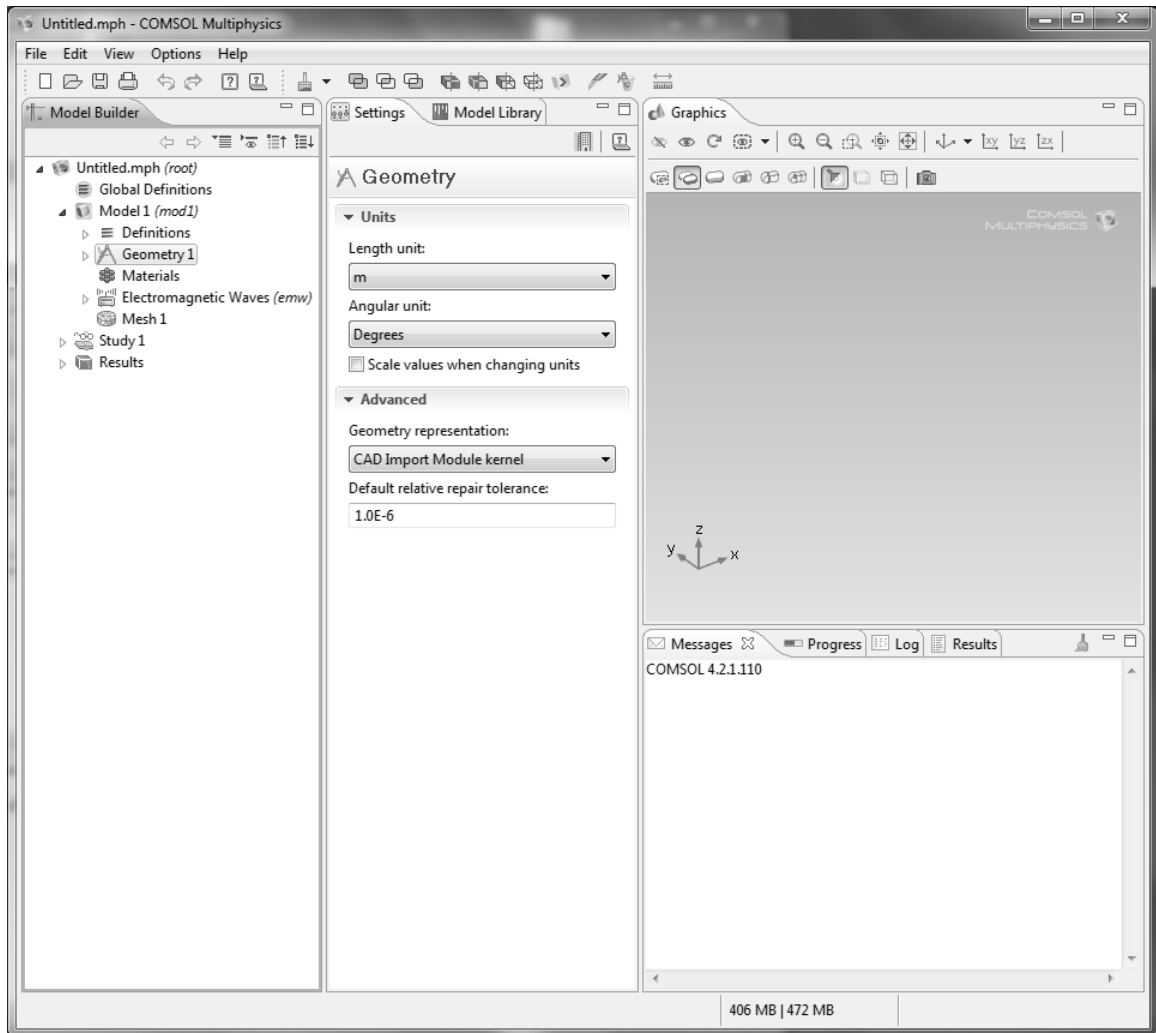


**Figure B1. Basic RF coil model**

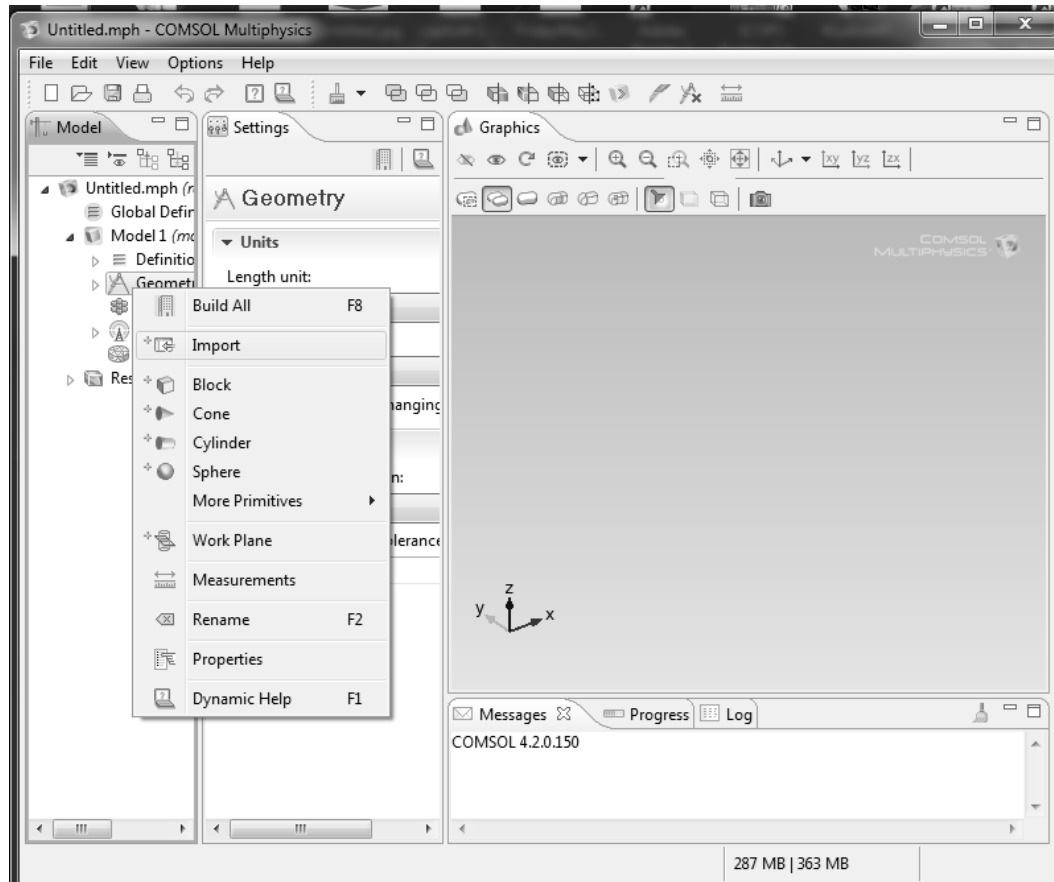


**Figure B2. Example of right-clicking while hovering over “Geometry” to show the import option**

### Geometry and Selection

After importing the SolidWorks file, a sphere is added with a layer to act as the perfectly matched layer. Next, the work plane is selected and a rectangle added to become the lumped port as shown in Figure B3. Finally, a cylinder is added around the antenna to be simulated as LTCC.

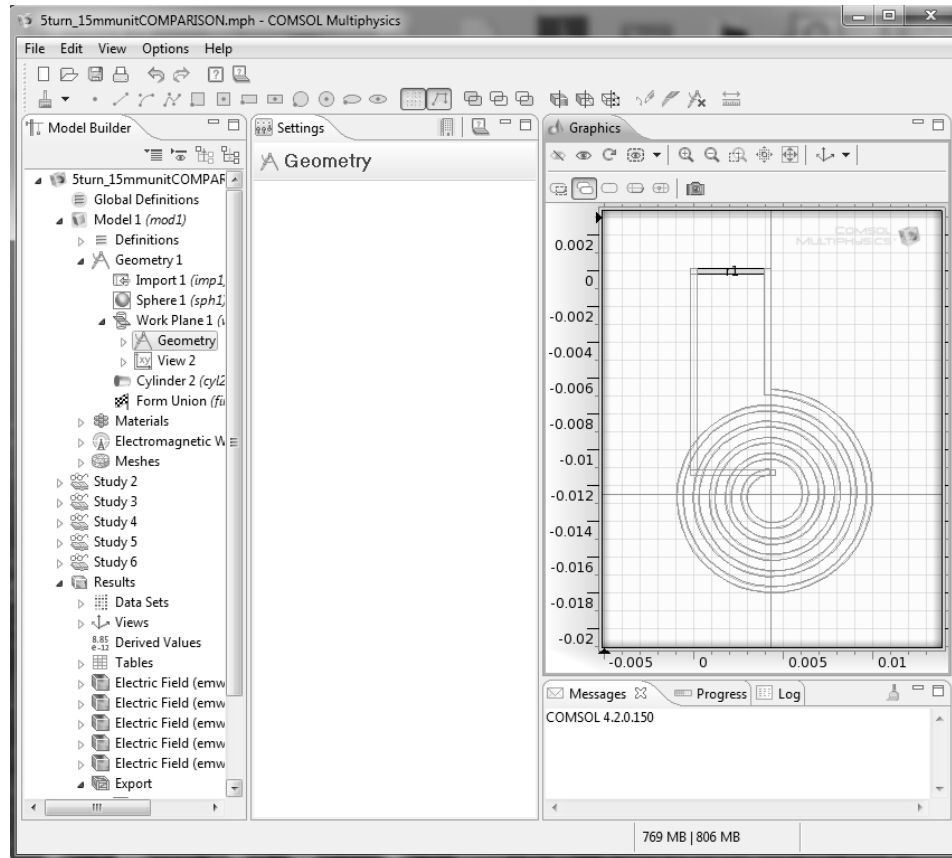


**Figure B3. Creating the rectangle to be used as the lumped port**

Next an Explicit Selection was created, consisting of all the external boundaries on the SolidWorks import file. This selection was named Coil Surface.

### Materials

The behavior of LTCC is added in the physics section, so only two materials were needed: air (defaulted to all domains), and a high conductivity material (copper). Copper was selected because it is a built-in material. Changing the conductivity to that of silver did not change the simulation results.

## Physics

The Electromagnetic Waves section defaults to have one wave equation, perfect electric conductor boundaries, and initial values of zero. Another wave equation was added to this section, with a loss tangent displacement field model. It used a relative permittivity of 7.8 and a loss tangent of 0.006 as shown in Figure B4. Next, the outer boundaries of the sphere in the model were set to be Perfect Magnetic Conductors, and the sections that make the outer layer of the sphere were set to be Perfectly Matched Layers. The Lumped Port was also designated as the rectangle constructed earlier, set to Uniform, Cable, On, 1 V, and 50  $\Omega$  characteristic impedance as shown in Figure B5.

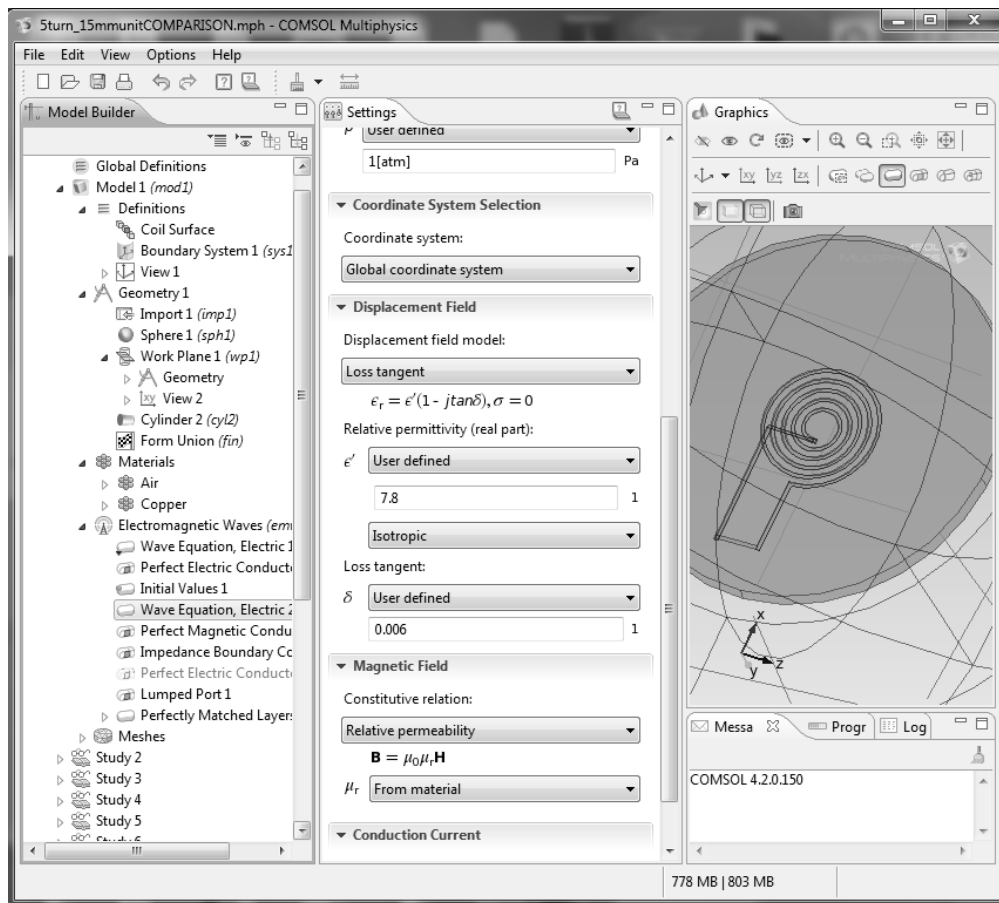
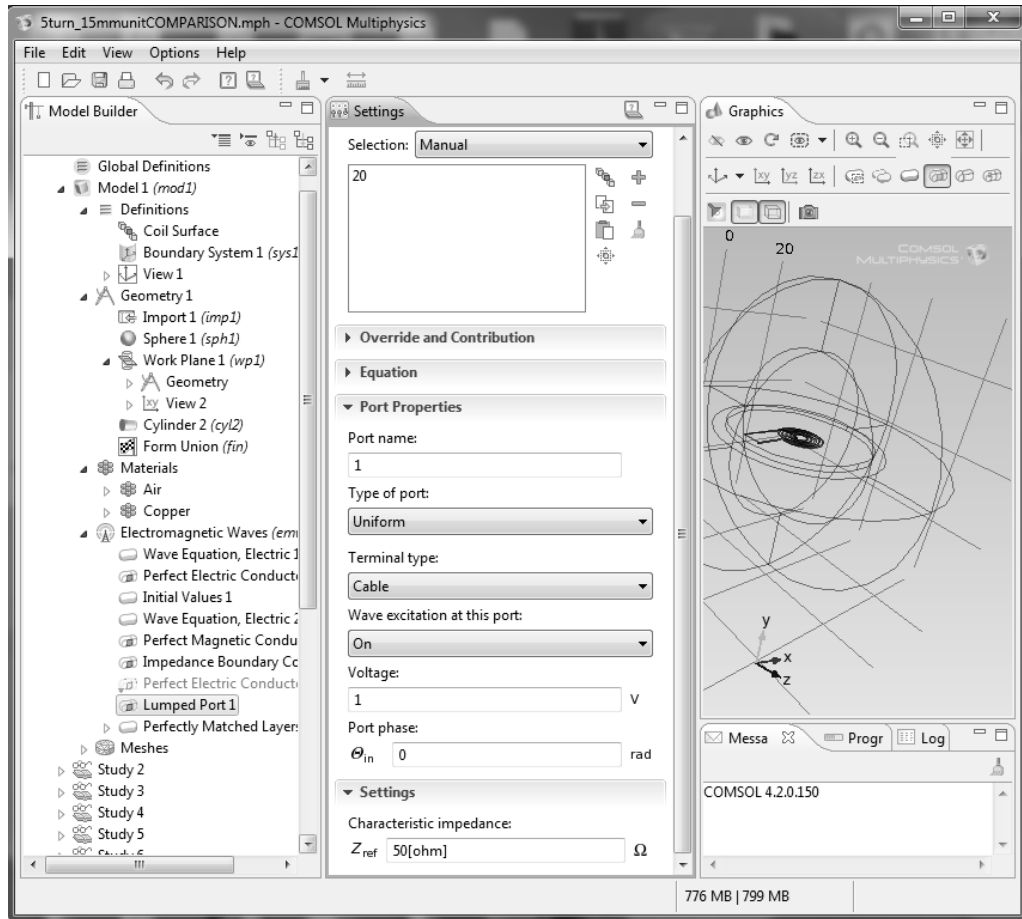


Figure B4. LTCC domain Wave Equation settings



**Figure B5. Lumped Port settings**

### Mesh

Finally, the design was meshed. A Free Tetrahedral mesh is used for every domain except for the outermost layer. The outermost layer is a swept mesh to ensure that the fields diminish properly in that region. In meshing, the goal was to achieve a mesh with less than 700,000 elements (the maximum solvable on the computer available) with reasonable quality as shown in Chapter 3. This required manipulating the size and other properties of the mesh for each domain. Oftentimes it was difficult to get the

geometry to mesh because of the fine features of the antenna relative to the overall geometry size, so trying many different mesh properties was required.

As a general rule, the “finer” the mesh selection, the smaller the minimum and maximum element sizes will be; the higher the resolution of narrow regions will be, and the lower the resolution of curvature will be. To obtain a mesh of reasonable size and quality for this project, a small element size is required with resolutions for a coarser mesh. An example showing one of the more difficult meshes (for antenna  $\beta$ ) is shown in Figure B6.

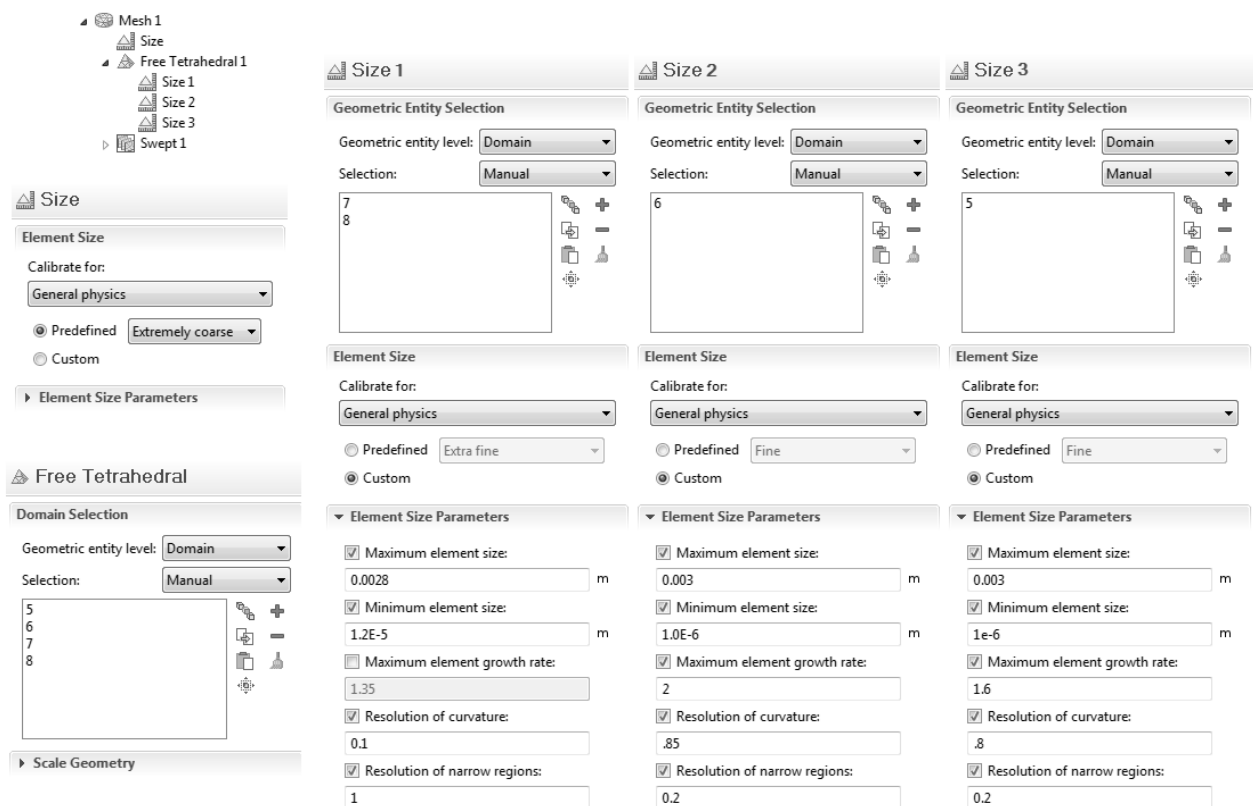


**Figure B6. Mesh details for antenna  $\beta$**

### Study and Results

Once the model was set, a **Study** was run to simulate the performance of the antenna for a range of frequencies. Then, a cut plane was created to show the intensities of the electric field vs. position. Data points were selected using **Cut Point**, and the data was exported. Figure B7 shows this portion of the process.

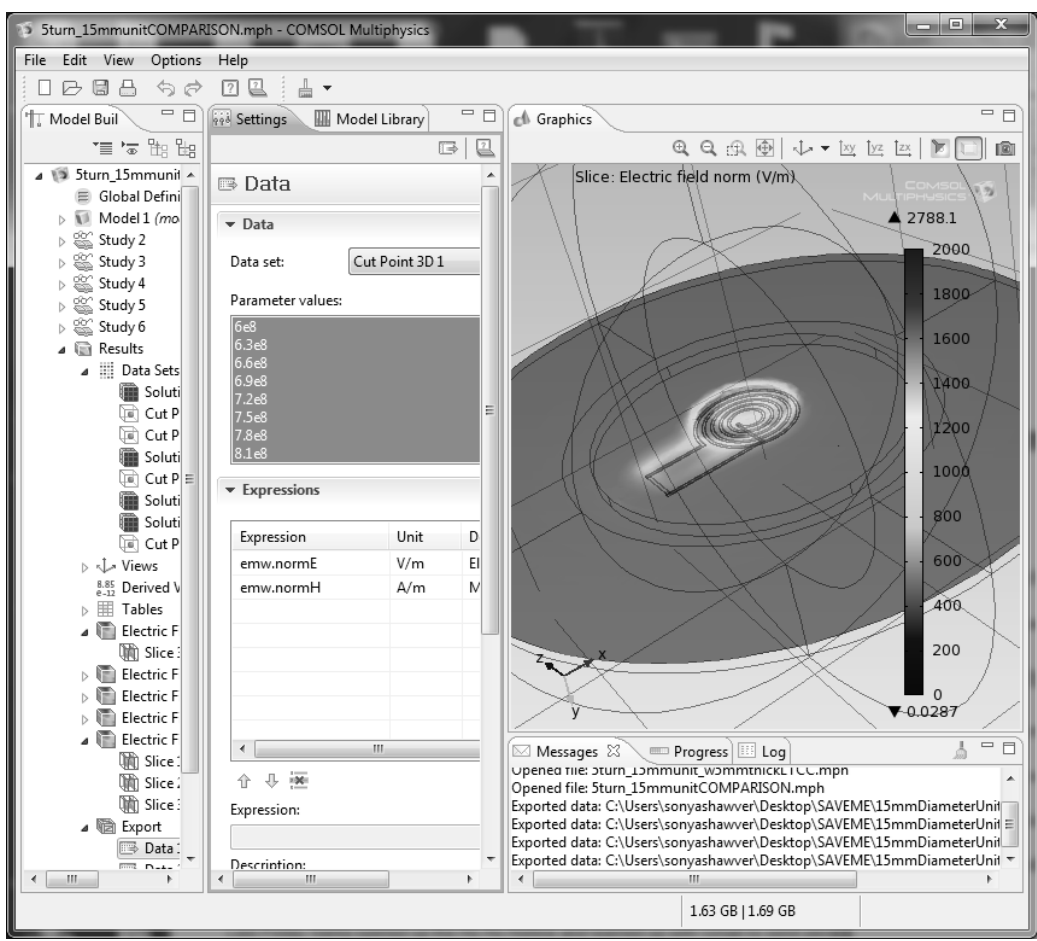


Figure B7. Viewing and exporting results



## APPENDIX C

## SolidWorks Antenna Model Development

Table C1: List of antennas simulated and fabricated

	pitch (mm)	# of turns
$\alpha$	0.9	5
$\beta$	0.78	8
$\gamma$	1.45	5

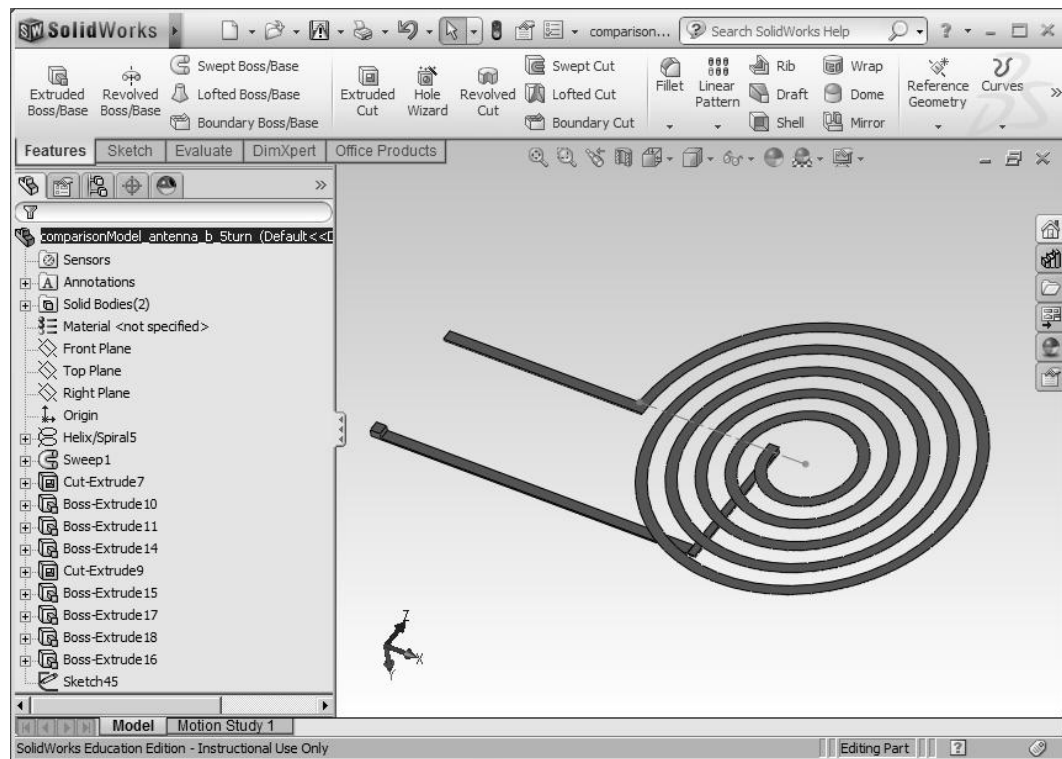


Figure C1. SolidWorks antenna development

To create the SolidWorks model of the antenna, first a spiral trace was constructed using the Helix/Spiral tool. Next, a Sweep was performed using a cross-section and the spiral trace. From there, the ends of the spiral were cut down to known angles and the traces to each side were created. Finally, the completed model was imported to COMSOL as a solid part file.

## APPENDIX D

## MATLAB Code

```

%|| A Sonya Shawver & Peter Bumbarger Production ||
%||
% -----
% Plots various Electric Fields of a Multi-turn spiral antenna modeled
% by concentric loop antennas of constant current and varying phase

function E_phi=MATLABsimForThesis(iter,myfrac, radii)
range=0;
lfrac=.1*iter+myfrac;
%calculate circumferences from radii
c=2*pi.*radii;
% Loop antenna circumferences [m]

lambda1=sum(c)/lfrac;
% One full-wavelength (like 900MHz)
k1=(2*pi)/lambda1;
% One wavelength wave number

%phase change
for n=1:length(radii)
p(n)=(c(n)*lfrac)*360/sum(c);
% Loop antenna 1 one-wavelength phase
end

I_0=1;
% Current through loop [A]
theta=linspace(0,2*pi);
% Angle around the z-axis on the xy plane *MATLAB defines this angle
differently from Balanis
phi=linspace(-pi/2,pi/2);
% Angle from the xy plane to the +z-axis *MATLAB defines this angle
differently from Balanis
[theta, phi]=meshgrid(theta, phi);
% Creates meshgrid
r=0.01;
% Observation distance from origin (small distances for near-field
approximation to work, r<<lambda) [m]

pshift=0;
E_phi=zeros(length(radii),100,100);

for n=1:length(radii)

```

```

    E_phi(n, :, :) = -
    li * ((radii(n) / sum(c)) ^ 2 * k1 * sum(c) * I_0 * (cosd(k1 * r + pshift) -
    li * sind(k1 * r + pshift))) / (4 * r ^ 2) .* sin(phi); % The E-Field in the phi
    direction (Eqn. (5-26d) from Balanis p. 241)
    pshift = pshift + p(n);
end
% *Note that theta and phi have been switched within the equation to
agree with MATLAB's coordinate system

E_phi0 = zeros(1, 100, 100);
% These equations are using the electrical length of one wavelength

for n = 1:length(radii)
    E_phi0 = E_phi0 + E_phi(n, :, :);
% Summation of the E-Fields of all the loop antennas
end

dim1 = ceil((length(radii) + 1) / 2);
dim2 = ceil((length(radii) + 1) / dim1);

subplot(2, 5, iter) % simply gets rid of need for index 1 in (1, h, q) so
sph2cart() may be applied
    for h = 1:100
        for q = 1:100
            E_phi0_new(h, q) = E_phi0(1, h, q);
        end
    end

% plot result
[x0, y0, z0] = sph2cart(theta, phi, abs(E_phi0_new));
surf(x0, y0, z0, 'EdgeColor', 'none')
view([0, 1, 0])
axis([-30, 30, -30, 30, -50, 50])
title(['\lambda ratio =', num2str(1/frac)], 'FontWeight',
'bold', 'FontSize', 13)

```